Remote Sensing of Environment 330 (2025) 114955

Contents lists available at ScienceDirect

Remote Sensing of Environment

journal homepage: www.elsevier.com/locate/rse

Global radio frequency interference in L-band SAR data from ALOS-1 and JERS-1 satellites

Yuhang Wang, Cunren Liang *, Fan Yang, Ligong Yang, Shangzong Lu, Xue Li, Qiming Zeng

Institute of Remote Sensing and Geographic Information System, School of Earth and Space Sciences, Peking University, Beijing 100871, China

ARTICLE INFO

Edited by Jing M. Chen

Keywords:
Radio frequency interference (RFI)
Synthetic aperture radar (SAR)
L-band
ALOS-1
JERS-1
Envisat

ABSTRACT

Synthetic Aperture Radar (SAR) data acquisition is increasingly challenged by the overcrowded radio frequency bands, leading to the problem of Radio Frequency Interference (RFI), particularly at L-band. Knowledges about global RFI are important for the protection of the microwave bands allocated for active remote sensing, SAR system design and operation, as well as the systematic mitigation of RFI for SAR data end users. It is becoming more important as we are entering the unprecedented golden age of L-band SAR satellites. In this work, we develop algorithms, workflow and system for operationally measuring global RFI experienced by L-band SAR data. We define a data format for recording the RFI measurements, which facilitates the computation of a number of RFI metrics. We process all available L-band SAR data acquired by the JAXA ALOS-1 (2006–2011) and JERS-1 (1992–1998) satellites. For comparison with RFI in C-band data, we also process part of the ESA Envisat (2002−2012) data archive acquired in the same time frame (2005–2007). The final results provide a global view of RFI at L-band, showing its spatial and temporal variations. We find heavy RFI pollutions in East Asia, North America, and the region consisting of Europe, North Africa and the Middle East. Comparison of results from ALOS-1 and JERS-1 indicates the increasing trend of RFI pollution. Comparison with C-band Envisat result shows that RFI at L-band is significantly more severe than at C-band. Comparison of results from different polarizations shows that cross polarization data are more susceptible to RFI due to their lower radar backscatter. The global RFI distribution from L-band SAR data is found similar to that from L-band passive radiometers including SMOS and SMAP.

1. Introduction

Synthetic Aperture Radar (SAR) is an active microwave remote sensing instrument that can acquire high resolution images of the Earth's surface. In the range direction, its resolution is attributable to its signal's wide bandwidth, usually covering several tens of megahertz. In addition to the signals transmitted by itself, SAR antenna also receives any signals from other sources transmitting electromagnetic waves in the same frequency band. These unexpected signals would degrade SAR images, which is known as Radio Frequency Interference (RFI). As the radio frequency bands are becoming overcrowded, RFI is increasingly affecting SAR signals, particularly at long-wavelength bands, such as L-band. L-band SAR plays a critical role in active remote sensing, with a variety of applications such as vegetation studies (Shimada et al., 2014; Chang et al., 2022), deformation measurement (Haghighi and Motagh, 2019; Liang et al., 2024), disasters monitoring (Grimaldi et al., 2020; Liu et al., 2021) and civilian surveillance (Arai et al., 2022). RFI is a potential threat to nearly all these applications.

The L-band a SAR can use ranges from 1215 to 1300 MHz, which is the frequency band the International Telecommunication Union (ITU) allocates to Earth Exploration-Satellite Service (EESS) (active). This frequency band is also allocated to Radio Navigation Satellite Service (RNSS), Radio Location Service (RLS), Space Research Service (SRS), Aeronautical Radio Navigation Service (ARNS), and amateur-satellite service. In some countries or regions (e.g. China and Japan), the shortage of spectrum resources has led to its repurposing for fixed and mobile services. RNSS, including Global Navigation Satellite Systems, Regional Navigation Satellite Systems, and Satellite-Based Augmentation Systems, is the primary source of spaceborne RFI in SAR data acquisition. The transmitted power of these interference signals is typically low, often only a few tens of watts (Spencer et al., 2013), but they are also continuous wideband coded signals, making them difficult to distinguish from SAR echoes. Ground-based RFI sources are more diverse, including RLS, telecommunications equipment for mobile or

* Corresponding author.
E-mail address: cunren.liang@pku.edu.cn (C. Liang).

https://doi.org/10.1016/j.rse.2025.114955
Received 26 January 2025; Received in revised form 29 July 2025; Accepted 2 August 2025
0034-4257/© 2025 Elsevier Inc. All rights are reserved, including those for text and data mining, AI training, and similar technologies.

fixed services, amateur radio, etc. The power of these RFI signals is often significantly higher than SAR echoes, and therefore they comprise the main interferences found in SAR data.

As the RFI issue is becoming more severe, it has been attracting increasing attention. For example, in 2010, the EC Joint Research Center conducted a study on the radio frequency threat against telecommunications and ICT control systems (Wildemeersch and Fortuny-Guasch, 2010). In the same year, the United States National Research Council (NRC) initiated a study addressing the challenges of radio frequency spectrum occupancy in passive microwave remote sensing (National Research Council, 2010). Five years later, NASA commissioned NRC to perform a similar investigation, focusing on active scientific sensors, particularly radar systems (National Academies of Sciences, Engineering, and Medicine, 2015). New Zealand (Chiang et al., 2007), India (Patil et al., 2011), China (Chen et al., 2012), and other regions have also conducted a series of spectrum occupancy analyses. Addressing the issue of RFI in SAR data requires a collaborative effort from the science community, government agencies, and the telecommunications industry.

Previous research on RFI in active microwave remote sensing has been mainly focused on algorithm development. Non-parametric methods primarily involve filtering and matrix operations. The former leverages the magnitude difference between RFI signals and SAR echo signals for RFI detection and mitigation (Buckreuss and Horn, 1998; Shimada, 2005; Chan et al., 2011; Meyer et al., 2013), while the latter makes use of techniques, such as principal component analysis (Zhou et al., 2013), eigenvalue decomposition (Yang et al., 2021), and subspace projection (Li et al., 2022), to directly separate interference signals from SAR signals. Non-parametric methods usually lead to signal loss. Using both magnitude and phase information, parametric methods first try to model the RFI signals and then estimate the model parameters (Miller et al., 1995; Huang and Liang, 1999; Liu et al., 2013; Mao et al., 2024). Parametric methods aim to preserve SAR signal while mitigating RFI. However, as the RFI signals are diverse and may even be complex, accurate modeling of each type of RFI is challenging. To improve the interference suppression performance while retaining the SAR echoes, the signal separation problem has been transformed into an optimization problem. This leads to the semi-parametric methods based on "low-rank" and "sparse" properties (Nguyen and Tran, 2016; Liu et al., 2018; Lu et al., 2021; Lyu et al., 2021; Su et al., 2022). These algorithms require tuning of one or more hyperparameters based on prior knowledge of RFI and SAR signal characteristics, which is why they are classified as semi-parametric methods. In recent years, machine learning techniques have also been explored for RFI detection and mitigation (Artiemjew et al., 2020; Tao et al., 2022; Sorensen et al., 2023). These methods can also be classified as semi-parametric since they integrate data-driven pattern recognition with predefined model architectures and manually-tuned hyperparameters. However, both optimization and machine learning approaches entail significant computational burdens due to their iterative nature and high-dimensional parameter spaces.

While the algorithms continue to improve particularly considering the diversity of RFI sources, there is also a growing need of RFI database to support the analysis of global RFI, the engineering and science applications, and the policy making for protecting the radio frequency bands allocated to microwave remote sensing (Spencer and Ulaby, 2016; De Matthaeis et al., 2018; Pedro et al., 2022). In passive microwave remote sensing, global RFI products have already been routinely generated and analyzed for L-band microwave radiometers including those onboard SMAP and SMOS satellites (Mohammed et al., 2016; Oliva et al., 2016; Uranga et al., 2018), which indeed has helped protect the frequency band allocated to passive microwave remote sensing. In active remote sensing, however, much less effort has been put into the systematic generation, archiving, and analysis of the global RFI. In Meyer et al. (2011), a very preliminary version of global RFI from ALOS-1 data was generated with limited temporal coverage (2010 to 2011). For satellite operation agencies, such as Japan Aerospace Exploration Agency (JAXA), their work has been mainly focused on the removal of the RFI in the routine generation of SAR image products. A global RFI database along with its analysis become particularly important, as we are entering the golden age of L-band SAR satellites with a fleet of L-band SAR satellites in operation and to launch in the future including ALOS-2, SAOCOM-1 A/B, LuTan-1 A/B, ALOS-4, NISAR and ROSE-L.

In this work, we develop algorithms, workflow and system for operationally mapping the global RFI in L-band SAR data. We define a data format for recording the RFI measurements, which facilitates the computation of a number of RFI metrics. We process all available L-band SAR data acquired by the JAXA ALOS-1 (2006–2011) and JERS-1 (1992–1998) satellites. For comparison with RFI in C-band data, we also process part of the ESA Envisat (2002–2012) data archive acquired in the same time frame (2005–2007). We also compare the results with those from L-band passive microwave radiometers onboard the SMOS and SMAP satellites. In the following sections, we present the results along with our analysis.

2. Method for measuring RFI

2.1. Workflow

Our purpose is to operationally and systematically process the entire data archive acquired by different satellites. First of all, the RFI measuring method should be efficient enough to allow us to handle such large amount of data. Secondly, the method should be robust enough to effectively deal with different situations.

Our workflow for measuring RFI is shown in Fig. 1. The workflow works with raw data and processes the data orbit by orbit. The data of an orbit may consist of several blocks of data in azimuth depending on the SAR operation periods in the orbit. For each block, the data are segmented into a number of smaller blocks in azimuth, with each smaller block having the same starting range. Each smaller block is further segmented into even smaller manageable blocks in azimuth, hereafter referred to as subblocks, so that the data volume won't exceed the computer capacity. The RFI measurement algorithm works on the subblocks in the range frequency domain. The subblock processing results are then geocoded using SAR geometry and estimated Doppler frequency parameters, forming the result of a whole original block that is not segmented.

2.2. Preprocessing of the data

For a SAR satellite, the whole Earth's surface is divided into standard tracks and frames, and the data are distributed according to the track and frame numbers. We manage the large amount of SAR data according to their orbit numbers, however. When SAR orbits around the Earth, it may turn on and off a few times, and therefore the data acquired in one orbit may consist of a few continuous blocks. Each block can cover a number of consecutive frames in azimuth. During the acquisition of the block of data, the starting range can change every short period of time.

For each block of data, we first stitch the frames in the block, and then segment the entire block into smaller blocks in azimuth based on starting ranges. Note that the overlapping areas between two consecutive frames are large (e.g. 17,000–18,000 lines for ALOS-1) considering the long synthetic aperture of L-band SAR. This approach can avoid the redundant processing of the overlapping areas and the range zero-padding due to the change of starting range, and facilitate the Doppler centroid frequency estimation and the positioning of detected RFI. The resulting smaller blocks are actually large. For example, the mean smaller block length of ALOS-1 is about 60,000 lines. Therefore, each resulting smaller block is further segmented into subblocks with a length of 5000 lines, so that they can be easily handled by a computer.

We want to measure all RFI in the bandwidth spanning the range sampling frequency, rather than only the range bandwidth. However, the actual range spectrum magnitude varies within this frequency range,

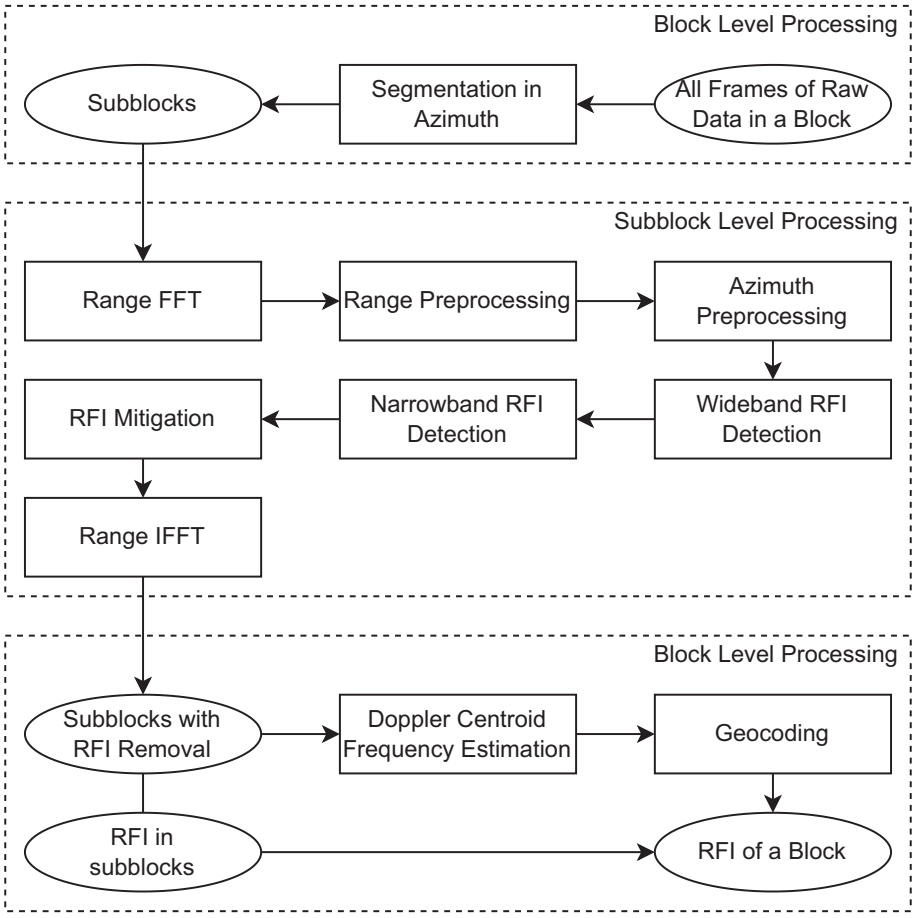

Fig. 1. The workflow for operationally measuring global RFI in L-band SAR data.

affecting the detection of RFI. On the other hand, there is a null area in the spectrum associated with the oversampling ratio of the data. Ideally, the magnitude of the range spectrum is a rectangular function. The actual spectrum magnitude, however, depends on the specific SAR instrument and the Gibbs phenomenon.

To remove these fluctuations of the spectrum, we first estimate a standard spectrum using data acquired in RFI-free areas whose backscatter does not change with range frequency. We use a large amount of data acquired in South Africa, South America, and over oceans, compute their range spectra, and average these spectra to estimate the standard spectrum. The normalized standard spectrum of ALOS-1 FBD mode is shown in Fig. 2.

The Gibbs phenomenon is removed by dividing the range spectrum by the standard range spectrum. In the null area of the spectrum, however, the estimated standard spectrum may not be representative depending on noise levels. For this part of the spectrum, we use polynomial fitting to capture and subsequently remove the spectrum magnitude variations. A quartic polynomial can reach a correlation coefficient as high as 0.999, and thus is enough to remove the variations. Fig. S1 in the supplementary materials shows a result of removing the spectrum magnitude fluctuations for ALOS-1 FBD mode data.

As a final problem of the range spectrum, the zero-frequency magnitude appears abnormally high for some data (e.g. data of ALOS-1 FBD) as shown in Fig. S1 in the supplementary materials. This is not RFI. It is caused by the use of nominal bias values for the I and Q channels. For ALOS-1 FBD mode, both I and Q biases are 63.5. If we use the I and Q biases estimated as the mean value of each channel instead, the large magnitude of zero frequency disappears as shown in Fig. S2 in the supplementary materials. However, the estimated value might still not be precise enough as there is still a smaller anomaly at zero

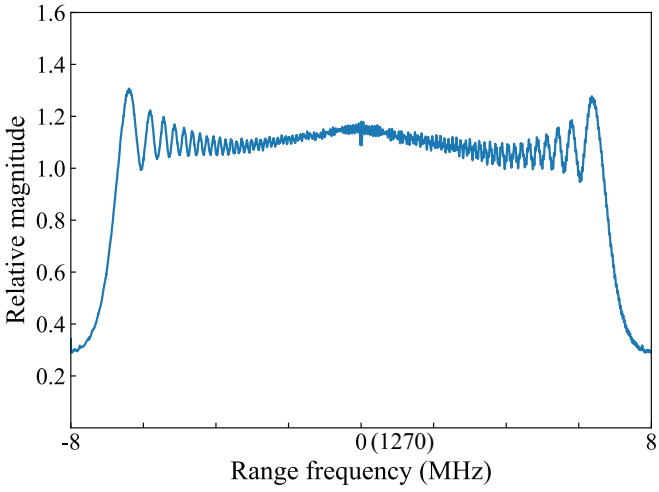

Fig. 2. The normalized standard spectrum of ALOS-1 FBD mode. The number in the parentheses in the horizontal axis represents the actual radar center frequency, and the same applies to the subsequent figures.

frequency. This smaller anomaly is caused by the bias in the mean value due to the RFI.

In azimuth, the magnitude of the radar echo varies with different landcovers. We use a Gaussian filter to suppress the variations to minimize their effects on the RFI measurement. The filtering is performed on the mean magnitude of each line. However, due to the presence of RFI, the computed mean magnitude also deviates from its true value. If the

number of lines is large, the characteristics of RFI, such as bandwidth and power, may change significantly, leading to substantial deviation differences and therefore a decreased accuracy of RFI detection. This constraint is also one of the reasons why we limit the number of lines in each subblock to 5000.

2.3. RFI detection

In general, RFI detection techniques mainly identify the presence of signals significantly different from the expected radar echo return, either in the frequency or time domain. According to the National Academies of Sciences, Engineering, and Medicine (2015), RFI is classified as narrowband RFI, pulsed RFI, broadband RFI and heterogeneous RFI environments. Narrowband interference typically has a bandwidth significantly narrower than the operational bandwidth of the SAR system while maintaining temporal continuity relative to the sensor integration time. Pulsed RFI often exhibits intermittent temporal characteristics with varying repetition intervals, occupying a wider bandwidth compared to narrowband RFI. These two categories constitute the predominant RFI signals in SAR datasets and are the primary targets of most RFI detection algorithms (Tao et al., 2019). Broadband RFI encompasses signals modulated over bandwidths comparable to or exceeding the SAR system's operational bandwidth, and is usually continuous in time. Heterogeneous RFI involves concurrent emissions from multiple RFI sources exhibiting diverse temporal-spectral characteristics. The latter two categories prove particularly challenging to distinguish from SAR echoes due to spectral overlap and temporal coexistence.

No algorithms are able to detect all types of RFI considering the diversity. To detect global RFI, efficiency should also be considered. An operational algorithm thus have to be both computationally efficient and effective for most RFI. Meyer et al. (2013) detected the first two types of RFI and renamed them as time-stationary narrowband RFI and time-varying wideband RFI, better reflecting their distinct temporal-spectral characteristics. We also detect these two types of RFI, which appears as vertical or horizontal bright lines in the range frequency and azimuth time domain. We hereafter refer to them as narrowband RFI and wideband RFI respectively.

In the range frequency domain, the spectra of RFI and radar echoes are superimposed, and therefore the magnitudes of spectrum components containing RFI are larger than those without RFI. We compute the mean value and standard deviation of the spectrum magnitude and then set a threshold as the mean value plus three times the standard deviation. Pixels with magnitude above this threshold are identified as containing RFI. This process is iterated twice considering the significant bias in the initial estimation result. RFI with lower power thus cannot be detected.

We execute the detection in both row and column directions, corresponding to wideband RFI and narrowband RFI with a long time span, respectively. For wideband RFI detection, the range frequency spectrum is divided into a number of frequency bands with a 50% overlap between adjacent bands. Within each frequency band, the previously described method is used to identify pixels contaminated by RFI. Narrowband RFI detection involves dividing the data into a number of pieces along the azimuth direction and applying a similar approach. During narrowband RFI detection, the results from wideband RFI detection are taken into account to avoid extensive overlaps between the two types of RFI.

During wideband RFI detection, there may be frequency bands that are heavily affected by RFI, such as those near the center frequency shown in Fig. S3(a) in the supplementary materials. In this case, the computed mean magnitude may not accurately represent that of radar signal without RFI. Therefore, it is necessary to consider the computed mean magnitudes of all frequency bands collectively and conduct a cluster analysis, assuming that frequency bands with large mean magnitudes have higher RFI. We apply the k-means method, sequentially testing the number of clusters from 2 to 4, and select the classification scheme with the highest silhouette coefficient. The RFI level in frequency bands differs significantly in different classes. For frequency bands with higher RFI, their parameters, including both mean value and standard deviation of the spectrum magnitude, are replaced with those of the frequency bands in the class with the lowest RFI.

For narrowband RFI detection, the data are divided into a number of pieces in the azimuth direction. If some pieces have high RFI that requires the aforementioned clustering analysis, it indicates that many narrowband RFI signals with different frequencies are received in a short period, which rarely happens. Even if it happens, these RFI signals would be detected as wideband RFI earlier. Therefore, we do not perform clustering analysis in narrowband RFI detection.

The detection algorithm generates discrete estimation results, which are refined using morphological dilation and erosion methods to form continuous results. The effect of morphological processing is shown in Fig. S4 in the supplementary materials. The continuous results not only better characterize the two types of RFI, but also facilitate the recording of detected RFI.

Pixels affected by RFI are set to zero to improve the Doppler centroid frequency estimation as required in the geocoding of RFI. Note that the preprocessing in range and azimuth is only for RFI detection. When removing RFI, the original spectrum should be used. Then the data are transformed back to the 2D time domain by a range IFFT, in which the subsequent Doppler centroid frequency estimation is performed.

2.4. Geocoding of the detected RFI

RFI Geocoding requires the radar antenna pointing direction, mainly the squint angle directly related to Doppler centroid frequency. For a block, we first estimate the Doppler centroid frequencies in each subblock, then we fit a 2D quadratic polynomial to the results. We use the phase increment method to estimate Doppler centroid frequency (Madsen, 1989). However, the PRF might change in a block. We estimate Doppler centroid frequency with data having the same PRF, instead of resampling the block to unify PRF. Therefore, when performing polynomial fitting, we use azimuth time, instead of azimuth line number.

Using the Doppler centroid frequency polynomial and radar geometric data as input, we geocode the RFI using the topo module in ISCE software (Rosen et al., 2012). To save time,

1) We use a constant elevation of 0 m, instead of a DEM.
2) We geocode the RFI subblock by subblock. For each subblock, we only run the topo module for the first and last lines. Results of the remaining lines can be obtained through interpolation.

To evaluate the position errors due to the use of zero elevation, we first generate a geocoding result for sample data using a real DEM with 30 m resolution. Then we repeat the process using DEMs of constant evaluations of 0, −500, and 9000 m, respectively. The resulting longitude and latitude errors are smaller than 0.02° and 0.005°, corresponding to a maximum position error of 2.5 km.

For the position errors due to the use of interpolation, note that the subblock size is only 5000 lines, and therefore the resulting errors should not be significant. We compare the interpolation results with geocoding results, and find the longitude and latitude errors are smaller than 0.008° and 0.002°, corresponding to a maximum position error of 1 km.

Note that our RFI detection algorithm is performed in the range frequency domain, making precise positioning in the range direction impossible. Given that the swath width is about several tens of kilometers, the errors caused by using zero elevation and interpolation are not significant.

2.5. RFI record format

We define a data format to efficiently and precisely record the measured RFI. Measured RFI of each block is saved in a separate file. The hierarchy of the file from top to bottom includes block, smaller block with same starting range and subblock. In each subblock, we record the mean intensity of the radar signal pixels unaffected by RFI for each line, and the mean intensity of each detected RFI and its starting and ending position indices. The mean intensity is computed as the mean value of the squared magnitude of the pixels in the range spectrum before pre-processing. The complete data format for recording RFI is provided in Appendix A. From the recorded information, we can easily reconstruct the range spectrum as shown in Fig. S5 in the supplementary materials.

With the defined RFI format, we can compute a number of metrics reflecting the impacts of RFI. Here, we focus on the percentage of RFI-affected pixels, the intensity ratio of RFI to SAR signal, and the total RFI intensity, all defined in each line. The total RFI intensity is computed as the sum of the squares of the magnitudes of RFI-affected pixels in the range frequency domain. By taking its mean value and dividing it by the mean intensity of the radar signal without RFI in each line, the intensity ratio of RFI to SAR signal can be obtained. When mapping the global RFI distribution, these metrics are presented at subblock level, using the mean value of these metrics across all lines in each subblock.

Unfortunately, the total RFI intensity is only a relative value, instead of an absolute value in unit such as Watt. It is difficult to obtain the absolute value as the associated system parameters are not available to us (See Appendix B). This prevents us from comparing RFI measurements from different satellites in an absolute sense. Nevertheless, the recorded RFI information can be easily converted to absolute RFI power once radar system parameters are available.

2.6. Performance of the RFI detection and mitigation

A comparison of the range spectrum before and after RFI mitigation is shown in Fig. 3. Our method detects RFI not only in the radar signal bandwidth, but also outside it. As shown in Fig. 4, an RFI extending across the two regions can be seamlessly detected, allowing the extraction of a complete RFI profile.

Interference signals are diverse, and a single method usually cannot detect all types of RFI. While RFI is mostly either narrowband or wideband signal, occasionally there are other types of RFI as shown in Fig. 5, which cannot be effectively detected. They are mostly RFI with irregular shapes in the range frequency and azimuth time domain. On the other hand, considering more types of RFI would sacrifice the efficiency of the detection, which is also important for the operational processing of the large amount of data.

After RFI detection, simply removing the frequency components polluted by RFI improves the image quality as shown in Fig. S6 in the supplementary materials. Data reconstruction methods such as linear prediction (Xu et al., 2020) and MIAA (Li et al., 2021) might have a better performance in improving the image quality, but they are beyond the scope of this research.

3. Data from different satellite missions and the associated problems

We process data from three satellite missions including JAXA's L-band ALOS-1 and JERS-1, and ESA's C-band Envisat. The C-band Envisat data acquired during the operation of ALOS-1 are used for comparison purposes. The important parameters of the data from the three missions are summarized in Table 1.

Fig. 6 shows the number of acquisitions for each dataset. The ALOS-1 and JERS-1 datasets include both ascending and descending passes, but we only use pass directions with more acquisitions (ascending for ALOS-1 and descending for JERS-1) to compute the number of observations. For ALOS-1 FBD mode, most areas have 2–8 observations, with a maximum of 19. There are more acquisitions in FBS mode, mainly for additional observations of Antarctica. For JERS-1, there are more acquisitions in Japan and its surrounding regions. For Envisat, we use data acquired from 2005 to 2007, aiming to achieve a global coverage while keeping the data volume to a minimum. Except for some regions in the Americas and Southern Africa that are not covered, all other regions have 1 to 4 coverages.

3.1. ALOS-1

The ALOS-1 satellite was launched on January 24, 2006, and stopped operation on May 12, 2011. The PALSAR radar onboard ALOS-1 can acquire data in different modes, but mostly uses FBD and FBS modes to acquire data. The FBD and FBS modes are therefore used for measuring the global RFI. The range bandwidth of FBS mode is twice that of FBD mode, and thus can detect more RFI at L-band. We use the data archived at the Alaska Satellite Facility (ASF). Part of the archive is only provided as Single Look Complex (SLC), and the RFI is already removed from the data (Japan Aerospace Exploration Agency, Earth Observation Research Center, 2008). These data cannot be used in our processing. With ALOS-1, we have 5 years of L-band RFI records.

3.2. JERS-1

The JERS-1 satellite was launched on February 11, 1992 and stopped operation on October 12, 1998. We downloaded all JERS-1 raw data

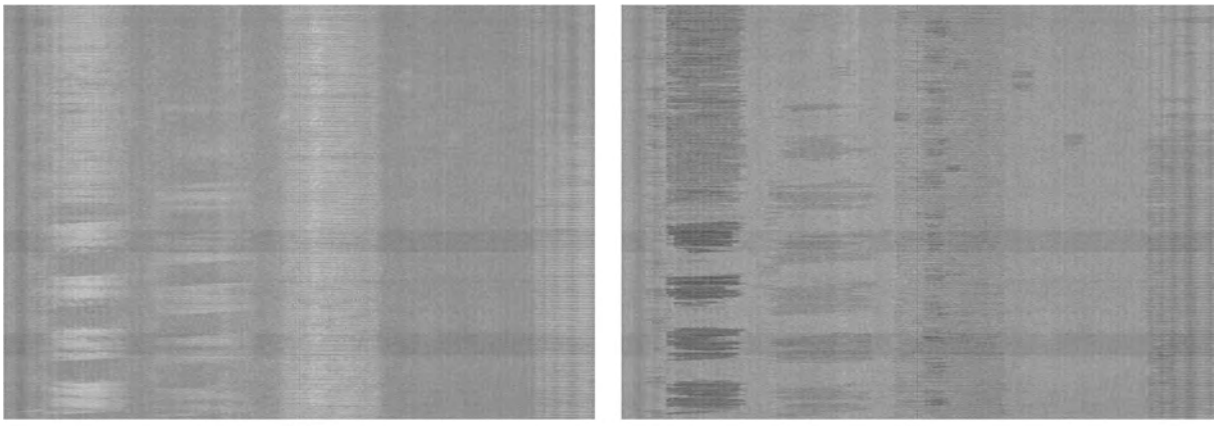

Fig. 3. (a) Original range spectrum. (b) Range spectrum after RFI mitigation.

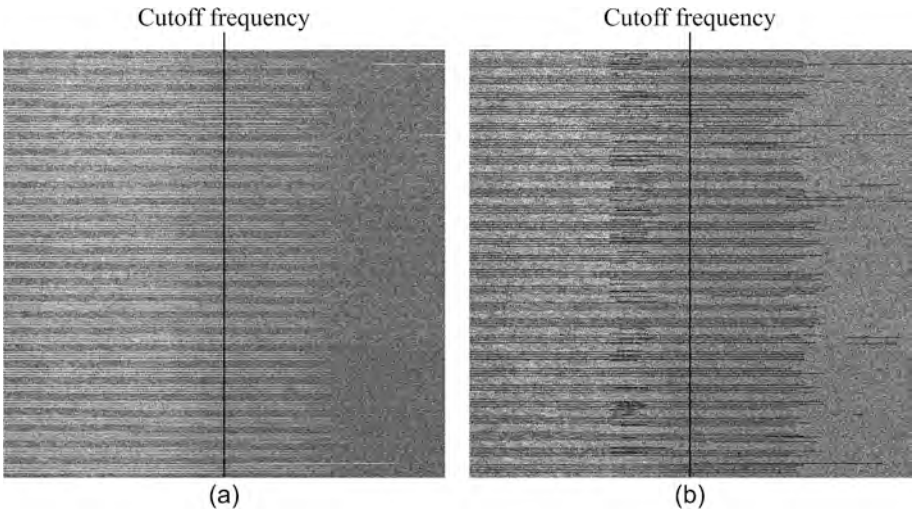

Fig. 4. RFI detection performance across range spectrum regions with and without radar signals. (a) Original range spectrum. (b) Range spectrum after RFI mitigation. The left side of the cutoff frequency represents the SAR signal, while the right side is outside the SAR bandwidth.

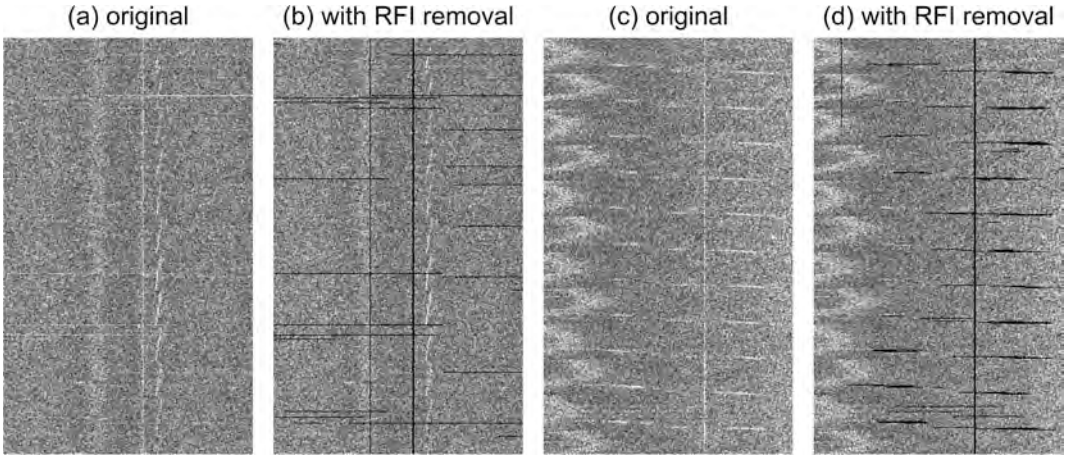

Fig. 5. The types of RFI that cannot be effectively detected.

using JAXA's G-Portal system. It extends the L-band RFI records by 6.5 years.

JERS-1 is a very early SAR satellite, and has various issues in its raw data. Of particular relevance to our processing are the abnormal starting range and PRF values as shown in Fig. S7 in the supplementary materials. To deal with these issues, we count the occurrences of each starting range or PRF value and record their start and end indices (i.e. the interval in which the value appears). If the value occurrences correspond to more than 40% of the frame length, or 80% of its occurrence interval and at least 10% of the frame length, it is considered as a valid value. Once valid values are identified, their occurrence intervals can also be determined. In cases where two adjacent intervals overlap, the boundary is determined based on the frequency of occurrence. For a gap between two intervals, the mean value in the gap is computed and replaced with the closest valid value. Additionally, the fact that the change in starting range is typically limited to a few hundred meters at a time can also be used as an additional constraint for restoring the true starting range.

Another problem is that some radar echoes do not seem normal as shown in Fig. S8 in the supplementary materials. They usually appear at the end of a frame with a significant jump of starting range. They are identified and not used in the RFI detection. In addition, sometimes there are missing lines in the raw data. Therefore, we add a separate field in the RFI record format for JERS-1 to record the number of valid lines in each subblock (see Appendix A), which helps characterize the data quality.

3.3. Envisat

Envisat was launched on March 1, 2002 and stopped operation on May 9, 2012. The C-band Advanced Synthetic Aperture Radar (ASAR) onboard the Envisat satellite can acquire data in 5 distinct modes. The mostly used one is the Image Mode (IM). The concurrent operation of Envisat and ALOS-1 provides us the opportunity to compare the RFI at C- and L-bands. However, ESA only allows users to access a limited amount of raw data. We use SLC instead.

We process part of the archive acquired in IM mode (swath IS2, VV polarization and descending track). We mainly process data acquired in 2007, achieving a maximum spatial coverage with minimum redundancy through careful selection of complete orbits. However, the data acquired in 2007 alone was insufficient for a global coverage. Therefore, we also use data from 2005 to 2006 to achieve a near global coverage.

For Envisat SLC, the radar signal and RFI energy is redistributed by azimuth focusing. We cannot directly use the aforementioned processing workflow to measure RFI. Before measuring RFI, we defocus the SLC using an inverse azimuth matched filter computed with parameters that are used to focus the raw data. We discard the incomplete convolution results at both ends of the data. A defocusing result is shown in Fig. S9 in the supplementary materials. The original SLC data provided by ESA

Table 1
Parameters of the satellite SAR data used.

	JERS-1	ALOS-1		Envisat
		FBD	FBS	
Date of First Acquisition Used	04/15/1992	05/16/2006		01/01/2005
Date of Last Acquisition Used	10/11/1998	04/02/2011		12/31/2007
Orbit Type	Noon-Night	Noon-Night		Noon-Night
Local Time on Descending Node	10:30–11:00 am	10:30 am ±15 min		10:00 am
Center Frequency	1.275 GHz	1.270 GHz		5.331 GHz
Transmit Power (peak power)	1.1–1.5 kW	2 kW		1.365 kW
Orbit Height	568 km	691.65 km		782 km
Look Angle	32°- 38°	9.9°, 21.5°, 34.3°, 41.5°, 50.8°		19.2°-26.7°
Swath Used	–	–		IS2
Swath Width	75 km	70 km		104.8 km
Range Bandwidth	15 MHz	14 MHz	28 MHz	16 MHz
Range Sampling Rate	17 MHz	16 MHz	32 MHz	19.2 MHz
Orbit Direction Used (Ascending/Descending)	A, D	A, D	A, D	D
Number of Frames Used	478,447	314,356	426,089	36,637
Number of Blocks Processed (i.e. Number of RFI Record Files)	23,268	9618	16,375	3896

typically has an overlap of more than 5000 lines between adjacent frames. Since the synthetic aperture length of the C-band ASAR corresponds to only about 1000–2000 data lines, there is still enough overlap between adjacent frames after defocusing. The defocused frames are stitched using time information. Note that unlike raw data, the starting range of each frame is fixed during focusing. We treat each frame as a smaller block, which are then divided into subblocks and processed with the previously described workflow.

4. Global RFI maps

Unless otherwise specified, the RFI distribution maps in this section show the mean values of the respective metrics computed using the number of acquisitions shown in Fig. 6 in Section 3.

4.1. ALOS-1 FBD mode

Although the ALOS-1 PALSAR acquires data on both ascending and descending orbits, there are significantly fewer acquisitions on descending orbits. We only present the RFI measurements from ascending orbits.

Fig. 7 shows the global distribution of RFI from ALOS-1 FBD mode data of different polarizations. The RFI in HV polarization data seems to be much more severe than that in HH polarization data. In fact, the L-band backscatter measurements from NASA/JPL AIRSAR data for a variety of landcovers (Freeman and Saatchi, 2004) indicate that the backscatter coefficient for almost all landcovers in HV polarization is weaker than the backscatter coefficient in HH polarization. Therefore, the signal power of cross-polarized imagery is lower than that of co-polarized data, which leads to a higher RFI-to-signal ratio, making RFI more pronounced (Meyer et al., 2013).

RFI is significantly more severe on oceans as shown in Fig. 7. This is primarily due to the very low backscattering strength on water surface. The intensity ratio of RFI to SAR signal is thus much larger than that on land, and therefore small RFI that would not be detectable on land can

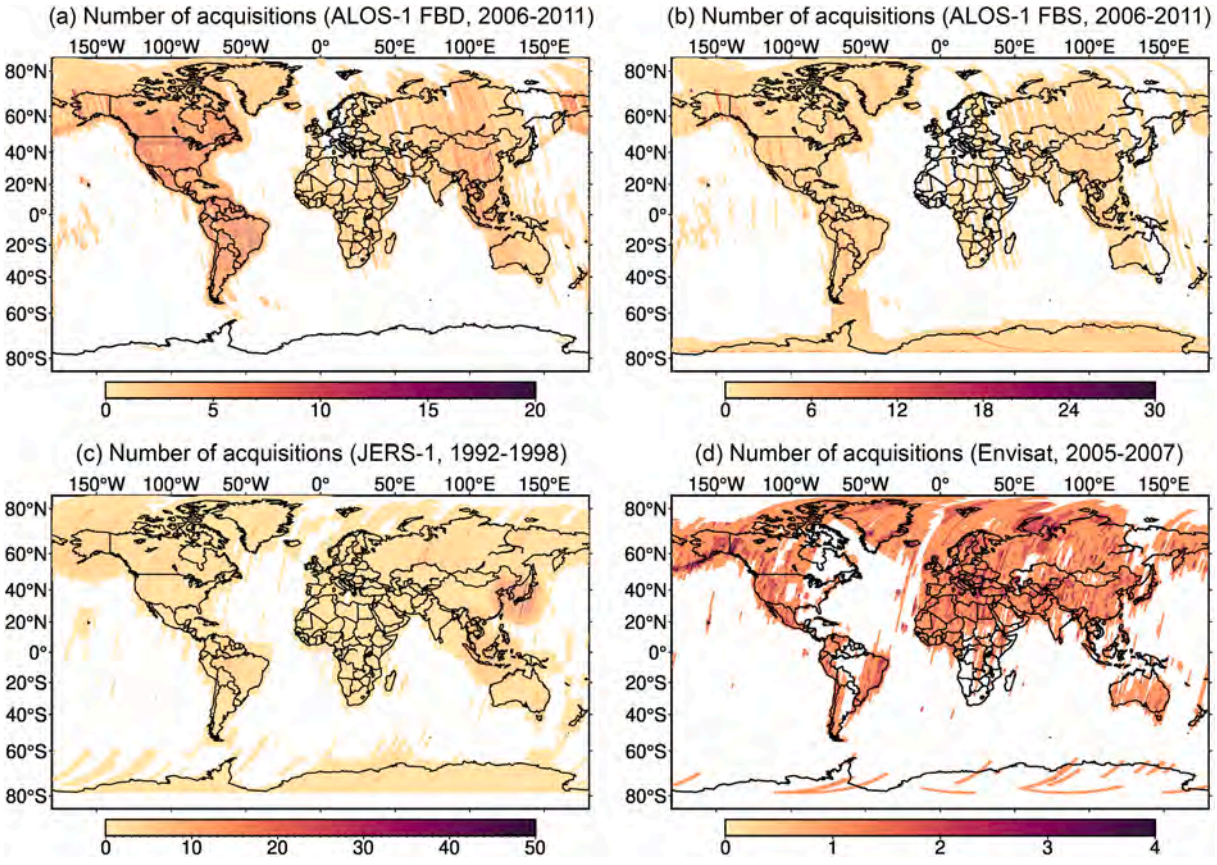

Fig. 6. Number of acquisitions of each dataset.

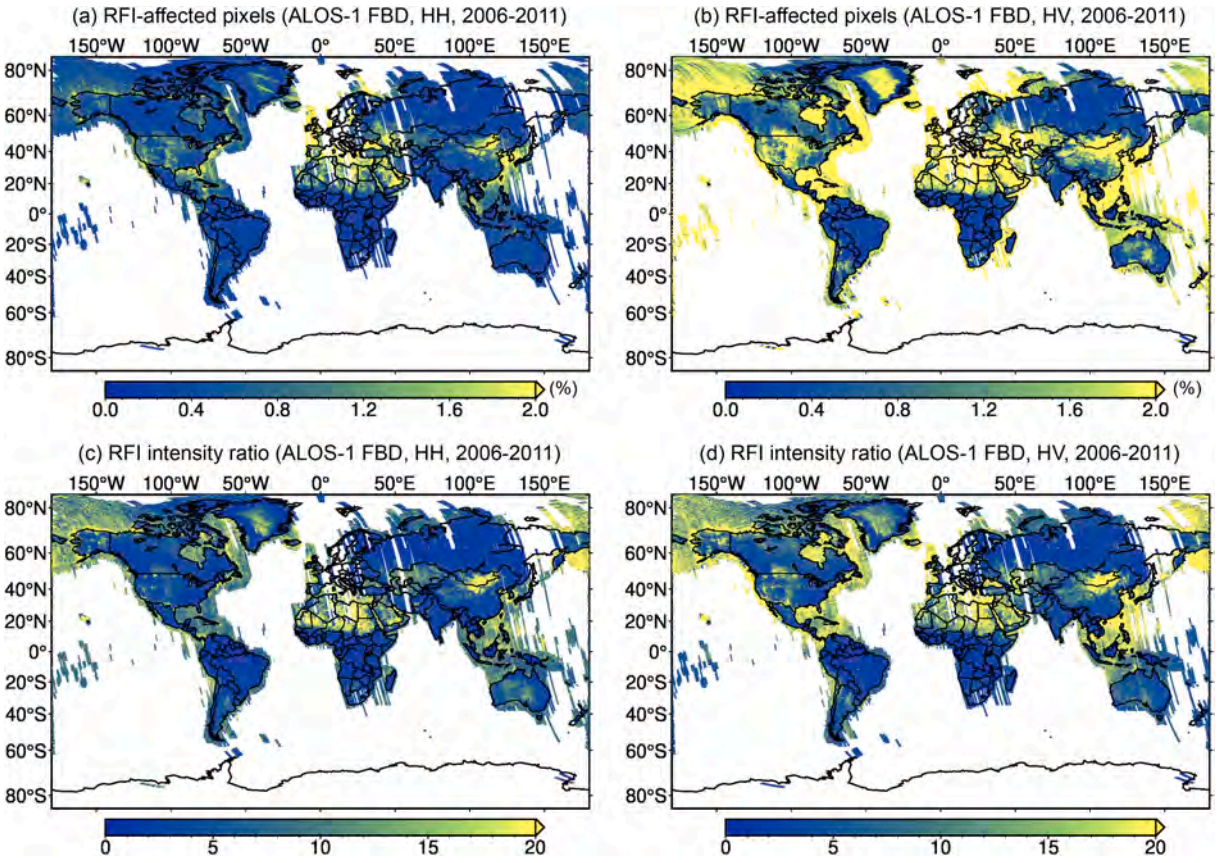

Fig. 7. The global RFI distribution maps from ALOS-1 FBD mode data, presented with two metrics including the percentage of RFI-affected pixels and the intensity ratio of RFI to SAR signal.

still be detected. Another possible reason is the strong specular reflection of RFI signal on the water surface. Therefore, we can see significant increase of RFI in both the percentage of RFI-affected pixels and the intensity ratio of RFI to SAR signal on oceans. Early results in Meyer et al. (2011) are also subject to this issue. Our third metric, total RFI intensity introduced later, can address this issue.

Fig. 7 reveals heavy RFI pollutions in three regions: East Asia, North America, and the region consisting of Europe, North Africa and the Middle East. The military conflicts in the Middle East might have contributed to the high levels of RFI. In Mongolia, preliminary results from the L-band LuTan-1 SAR satellite also reveal significant RFI (Chen et al., 2024). Furthermore, RFI in Mongolia has persistently been a major issue for the L-band passive SMOS mission (Kaihotsu et al., 2013; Oliva et al., 2016). The origins of these RFI emissions remain unknown. A comparison of the results from ALOS-1 and JERS-1 in Section 4.2 (e.g. Fig. 10) reveals that these RFI sources might have started to exist between the end of JERS-1 mission and the start of ALOS-1 mission.

Different from Middle East and Mongolia, the detected RFI in North Africa likely originates from Europe. In the RFI environment observed with the L-band passive SMAP mission (Bringer et al., 2018), the RFI sources in Africa are concentrated in Egypt, particularly near the border with Asia, with almost no RFI sources observed in other regions. Oliva et al. (2016) compared the RFI probability maps of SMOS for 2010 and 2014, clearly suggesting that RFI mitigation efforts in Europe significantly reduced the pollution observed in North Africa. In the results we generated, the percentage of RFI-affected pixels in Fig. 7(a) gradually decreases from Europe to North Africa. However, the intensity ratio of RFI to SAR signal does not follow this trend; instead, it is most pronounced in the Sahara Desert region of North Africa other than urban areas in Europe. This is due to the smaller dielectric constant in the dry desert, which leads to a lower radar backscatter. This phenomena further support the idea that RFI observed in North Africa mainly originates from Europe.

Fig. 8 shows the total RFI intensity in each line. The total intensity metric not only integrates the other two metrics, the percentage of RFI-affected pixels and the intensity ratio of RFI to SAR signal, but also incorporates the mean intensity of SAR signal, which depends on factors such as the surface backscattering coefficient (see Appendix B). It's difficult to compute total RFI intensity in absolute physical unit due to lack of knowledge about the radar systems (see also Appendix B), which adds to uncertainties in the comparisons across different datasets. However, total intensity provides a better representation of the actual RFI distribution, showing a more concentrated RFI distribution compared to the other two metrics. In particular, the maritime RFI is no longer clear and the concertation is moved to land. The RFI in North Africa has also been traced back to Europe, Egypt, and the Middle East.

In North America, the RFI hotspots arise from the Air Route Surveillance Radar (ARSR-4) along the continental United States border and the North Warning System (NWS) along the northern border of Alaska and Canada as shown in Fig. 9. Some of them are discussed in Meyer et al. (2013). These results also validate our RFI processing system.

4.2. ALOS-1 FBS mode and JERS-1

Fig. 10 shows the percentage of RFI-affected pixels and the intensity ratio of RFI to SAR signal for data acquired by ALOS-1 in FBS mode and JERS-1. The results of ALOS-1 FBS mode data in Fig. 10(a) and (c) show similar characteristics as those observed in FBD mode data. For the percentage of RFI-affected pixels, JERS-1 and ALOS-1 results show a high degree of consistency. In Antarctica, both ALOS-1 FBS and JERS-1 results contain a high proportion of pixels affected by RFI, which is an anomaly as explained in Section 4.3.

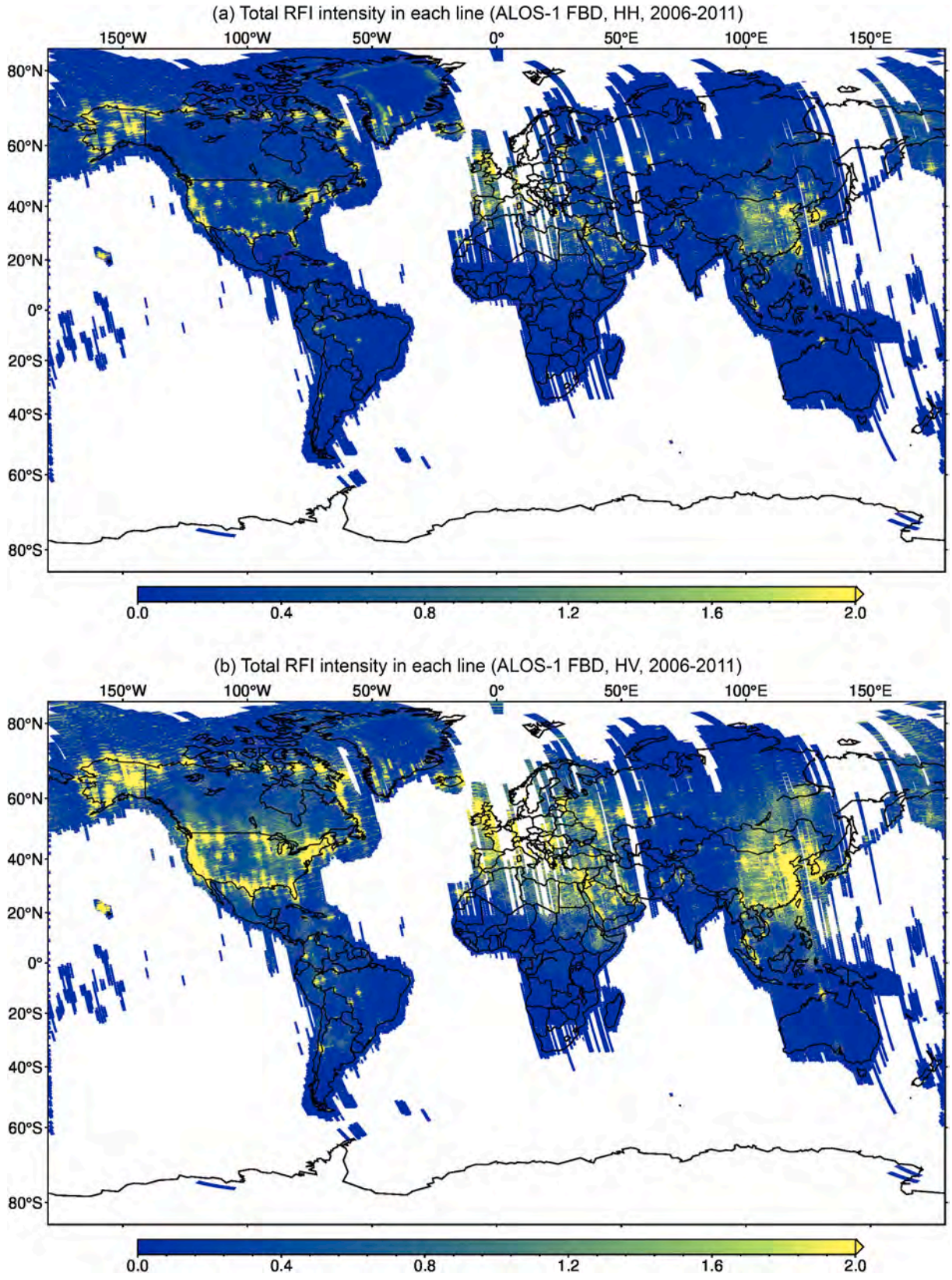

Fig. 8. The global RFI distribution map from ALOS-1 FBD mode data, shown as the total RFI intensity in each line.

In the percentage of RFI-affected pixels shown in Fig. 10(a) and (b), it seems that the RFI in JERS-1 data is more severe than that of ALOS-1 FBS mode data, which is not true. This is caused by a number of reasons. First of all, the transmission power of ALOS-1 is much larger than JERS-1, and thus less sensitive to RFI, which was also noted in the early ALOS-1 PALSAR Cal/Val summary (Shimada et al., 2007). Secondly, the higher percentage of RFI-affected pixels in JERS-1 is caused by more frequent false detections due to the poor quality of the JERS-1 data. The

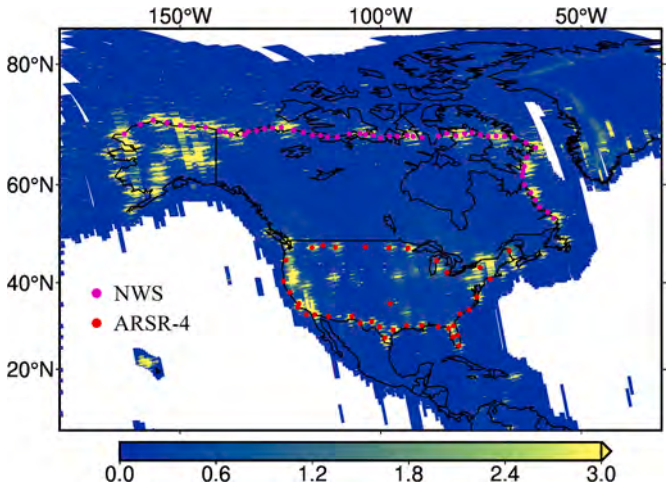

Fig. 9. RFI hotspots and the positions of the Air Route Surveillance Radar (ARSR-4) and the North Warning System (NWS) stations. ARSR-4 and NWS source: Wikipedia contributors, 2024a; Wikipedia contributors, 2024b.

missing lines in JERS-1 raw data can significantly affect the estimation of the mean SAR signal magnitude and its variance in RFI detection, leading to normal data near the missing lines mistakenly identified as interference. Another reason is the unstable JERS-1 range spectrum. The estimated "standard spectrum" is not applicable to some images. As a result, removing the Gibbs effect in these images may occasionally cause normal data to be misclassified as RFI. The intensity ratio of RFI to SAR signal in JERS-1 is lower than that in ALOS-1 as shown in Fig. 10(c) and (d), which also suggests that the higher RFI percentage of JERS-1 may be partially attributed to misdetection. The metric based on total RFI intensity proves superior again in this case, as normal data mistakenly identified as RFI generally have relatively low power. Mistakenly detected RFI does not stand out prominently on maps generated using this metric as shown in Fig. 11(b).

In Fig. 11, we can find the trend of increasing RFI pollution from the comparison of ALOS-1 and JERS-1 results, particularly in the continental United States and China. Although there are larger uncertainties in the cross-mission RFI comparison since we are not able to measure RFI in absolute physical unit, we can use the RFI caused by the NWS along the northern border of North America as reference. The construction of NWS was completed on July 31, 1957 (Lackenbauer et al., 2005), predating the operation periods of both ALOS-1 and JERS-1. In JERS-1 results, the RFI in the continental United States and China is much weaker compared to the RFI generated by NWS. However, for ALOS-1, the RFI in these two regions has become comparable to that of NWS. As shown in Fig. 9, the primary source of RFI in the continental United States is ARSR-4, which was promulgated in 1981, with building, testing, and evaluation taking place during the JERS-1 operation (Healy et al., 1997), and completed in May 2000 (FAA, 2002). Therefore, the RFI generated by the ARSR-4 is virtually absent in the JERS-1 results but is clearly noticeable in the ALOS-1 results. For China, although the RFI sources are unknown, the period between the end of JERS-1 operations and the start of ALOS-1 operations coincides with China's rapid development, which explains the changes in the observed RFI.

4.3. Envisat

Fig. 12(a)-(c) shows the RFI measurements from the C-band Envisat data. The RFI in C-band data is much lower than that in L-band, which is in agreement with other observations (Spencer and Ulaby, 2016).

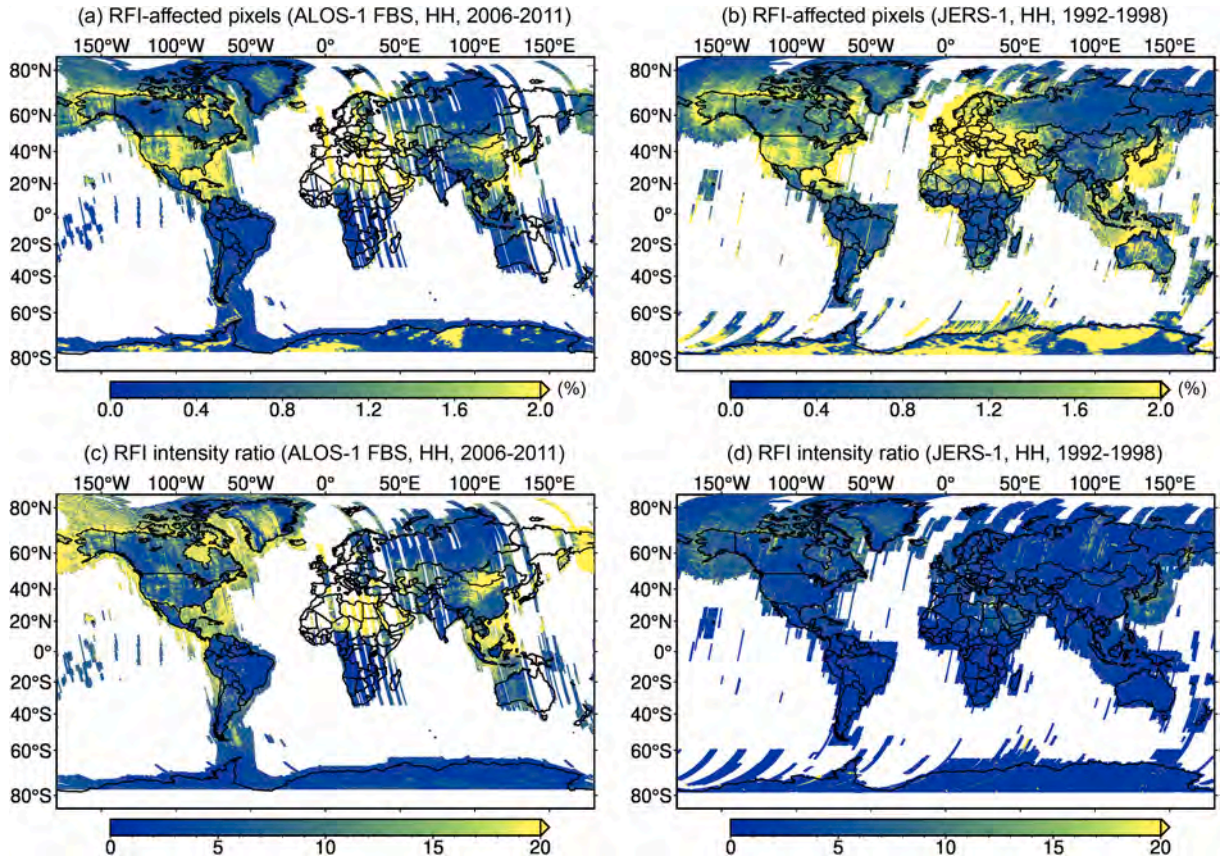

Fig. 10. The global RFI distribution maps from ALOS-1 FBS mode and JERS-1 data, presented with two metrics including the percentage of RFI-affected pixels and the intensity ratio of RFI to SAR signal.

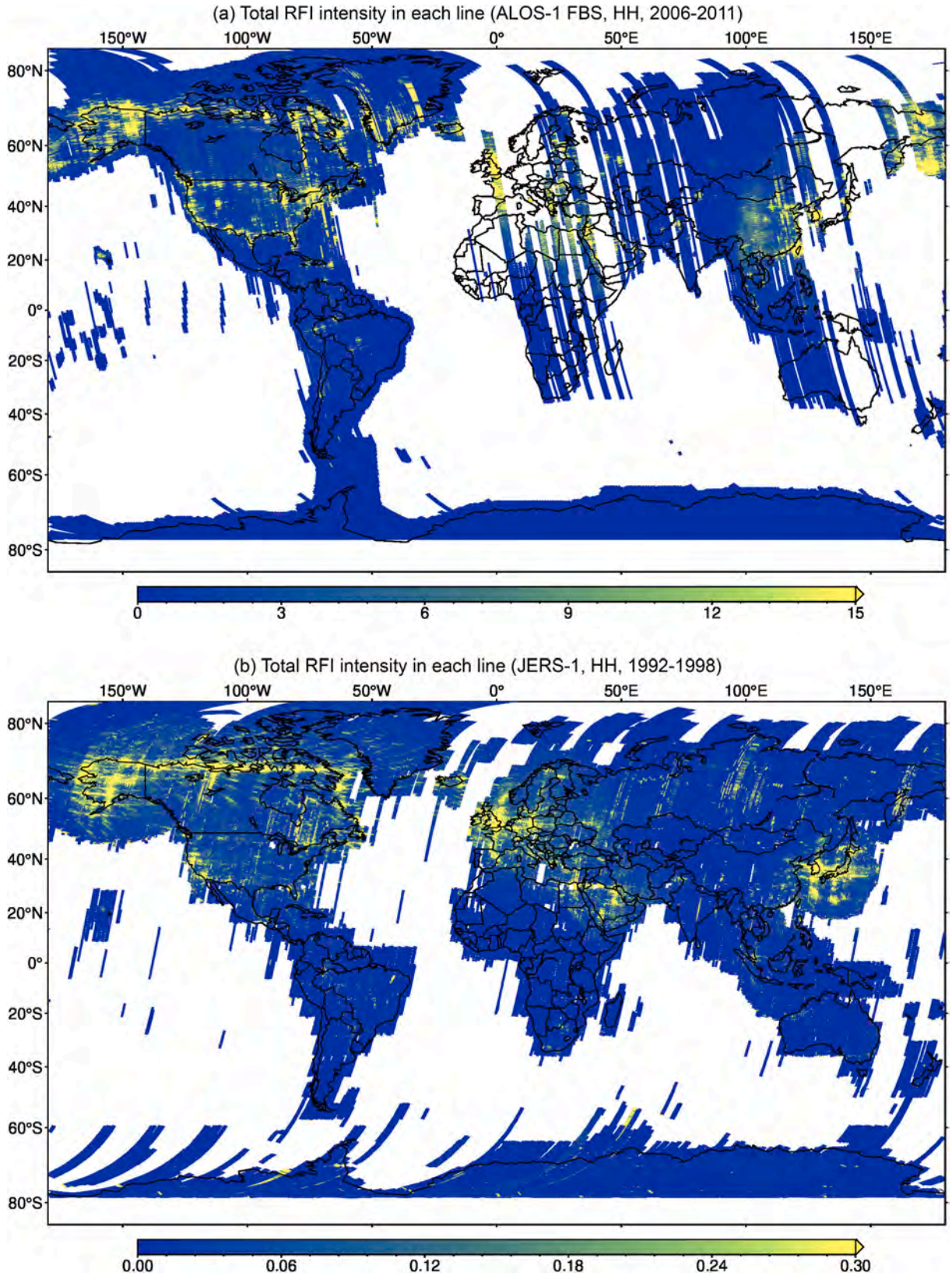

Fig. 11. The global RFI distribution map from ALOS-1 FBS mode and JERS-1 data, shown as the total RFI intensity in each line.

The high total RFI intensity along the margin of Greenland does not seem normal. In southern Greenland, RFI pollution was also found in data acquired by the C-band passive AMSR2 onboard the GCOM-W satellite (Parinussa et al., 2015). To further investigate this problem, we extract the mean intensity of the SAR signal with RFI removed from the RFI record file, which is shown in Fig. 12(d). The regions with high total RFI intensity are exactly those with high mean intensity of the SAR signal. According to Benson's (1960, page 153) classification of the

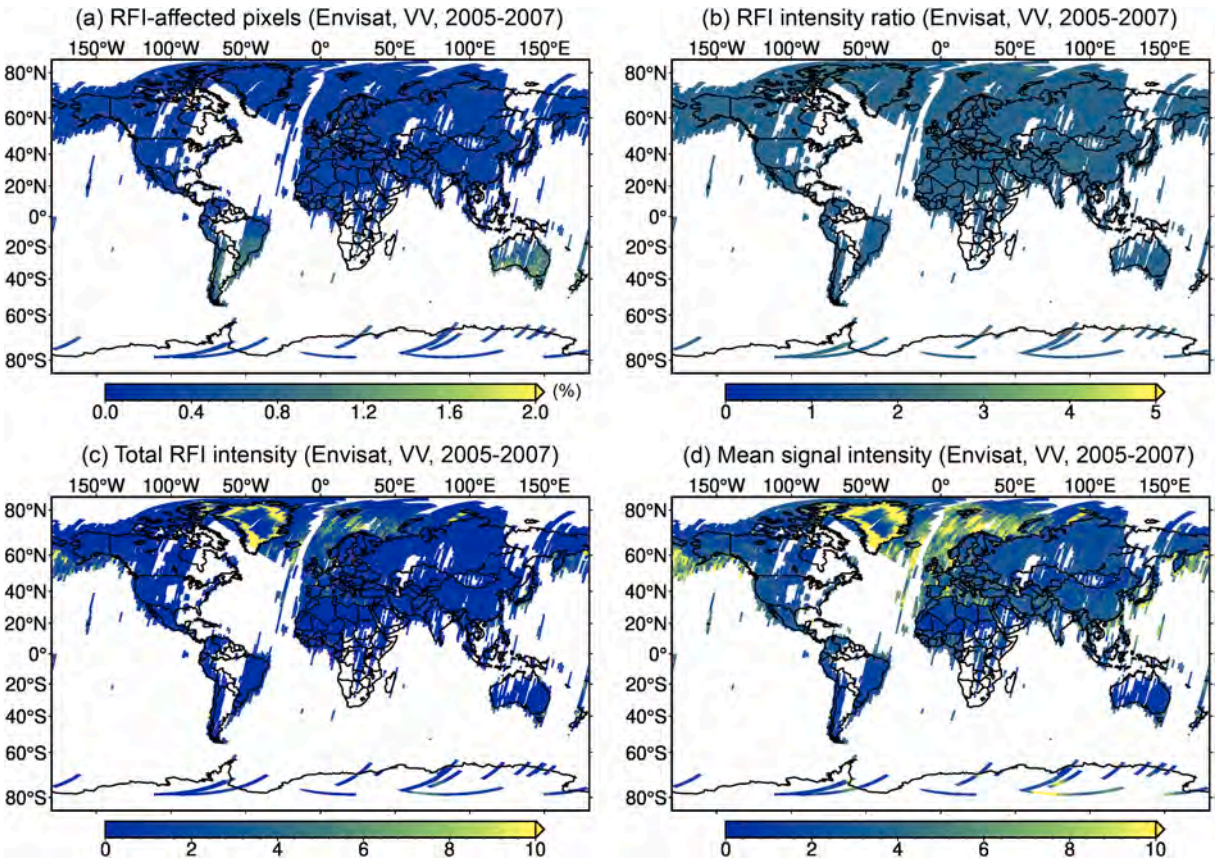

Fig. 12. The global RFI distribution map from Envisat data and the global mean intensity of the SAR signal with RFI removed.

Greenland ice sheet, the regions with low and high mean intensities correspond to the dry snow zone and percolation zone. The dry snow zone has a high elevation with minimal melting and thus smaller snow grains. This allows microwaves to penetrate deeper into the snow and to be absorbed, leading to small radar backscatter. In contrast, the percolation zone, where sublimation related to melting occurs, is covered by larger snow grains. During the summer melting period, the percolation zone may even form lens-like subsurface ice structures, leading to stronger backscatter (Ashcraft and Long, 2005). Therefore, much of the detected RFI is caused by false detections in this region. Zhao et al. (2013) used a multi-channel correlation method to mitigate the impacts of ice surfaces, but the method is not suitable for the data we use here. Therefore, RFI measurements in ice and snow regions should be treated with cautions.

The mean intensity of the SAR signal from L-band satellites in Fig. 13 is also higher in the percolation zone than in dry snow zone in Greenland. A similar pattern is observed in Antarctica, where regions with high radar backscatter coefficients are mostly those with longer annual melt periods (Fraser et al., 2016). The low backscatter of oceanic and desert regions mentioned in Section 4.1 is also clear in these results. However, the backscatter contrast between ice/snow and land surfaces at L-band is less pronounced than at C-band. Therefore, the L-band results in Greenland and Antarctica in Figs. 8 and 11 do not exhibit high total RFI intensity in areas with strong backscatter.

In the dry snow zones of Greenland and Antarctica, a high percentage of RFI-affected pixels is observed in L-band results. This is because the radar backscatter in the dry snow zone is very low. Besides, the backscattering mechanism of snow is complex, depending on particle size, frequency, incidence angle, azimuthal modulation, temporal change, etc. (Ashcraft and Long, 2005; Fraser et al., 2013). Therefore, the range spectra of these regions are of irregular shapes as shown in Fig. 14, significantly different from the standard spectrum shown in Fig. 2. This unexpected spectral response can easily cause a large portion of data in the frequency bands to be mistakenly detected as RFI, resulting in a high percentage of RFI-affected pixels. In Antarctica, RFI is mostly from false detections. In Greenland, however, there is indeed a certain amount of real RFI, because Greenland has a large and stable community, along with a relatively well-developed communication infrastructure (Andrews et al., 2021). The spectrum in the red box of Fig. 14(a) represents the RFI in Greenland. The higher intensity ratio of RFI to SAR signal in Greenland compared to Antarctica further corroborates this observation. The false detections in dry snow zones have low intensity, and thus are not clear in the maps representing total RFI intensity in each line shown in Figs. 8 and 11. The varying characteristics of false detections in different metrics were also found in the RFI-sensitive spectral difference indices computed using C-band passive AMSR-E data of dry snow zones in Greenland and Antarctica (Njoku et al., 2005).

4.4. Comparison with L-band passive microwave missions: SMAP and SMOS

Fig. 15 presents the earliest RFI results from two major L-band passive microwave remote sensing missions SMOS and SMAP, which are close to the operation time of ALOS-1. The central frequency of both SMOS and SMAP is the same, 1.4135 GHz, with a slight difference in bandwidth. The former has a bandwidth of 19 MHz, while the latter has a bandwidth of 24 MHz. Similar to the detected RFI in ALOS-1 data, East Asia and the region consisting of Europe, North Africa and the Middle East are again heavily polluted by RFI. Unlike these two regions, the pollution in North America is not heavy.

4.5. Variations with region and frequency

The occurrence of RFI apparently varies with regions, as well as

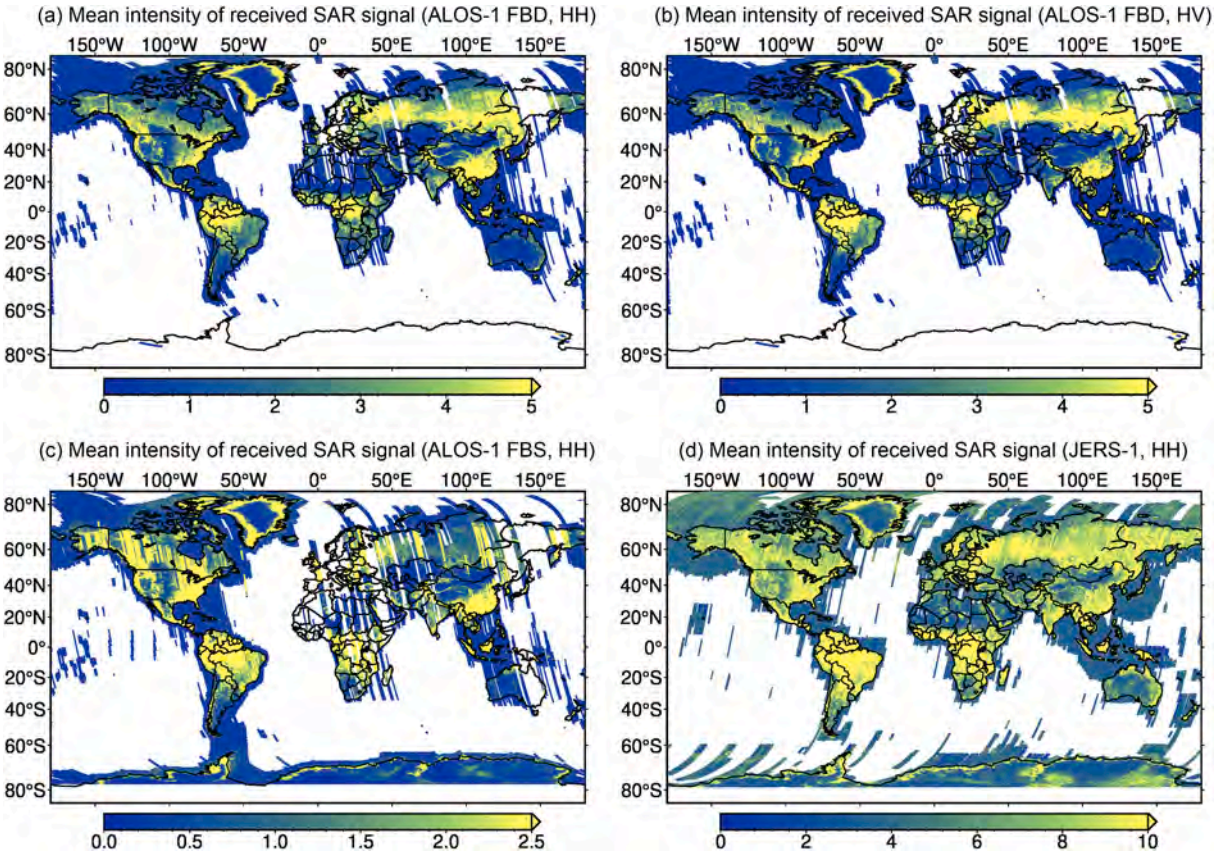

Fig. 13. Global mean intensity of the SAR signal with RFI removed from ALOS-1 and JERS-1.

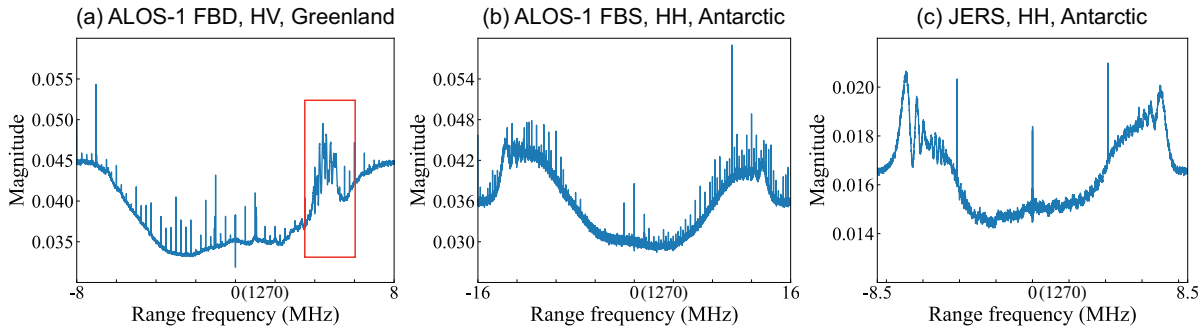

Fig. 14. Range spectra of L-band SAR data in Greenland and Antarctica. (a) Spectrum of a Greenland image (ALPSRP130691440-L1.0) acquired by ALOS-1 in FBD mode HV polarization. (b) Spectrum of an Antarctica image (ALPSRP028265680-L1.0) acquired by ALOS-1 in FBS mode HH polarization. (c) Spectrum of an Antarctica image (J1SAR19920903R02020607232431_0000G006) acquired by JERS-1 in HH polarization.

frequency bands. Again, the RFI record format greatly facilitates the analysis of these variations. Here, we analyze the RFI results derived from ALOS-1 FBD HH mode data. In measuring RFI, the original SAR data are transformed to the range frequency domain with an FFT length of 6144. We further compute the mean of every 8 samples. The 16 MHz sampling rate is then represented by 768 samples, with a sample size of about 21 kHz. As mentioned in Section 2.2, the magnitude at zero frequency, which represents the direct current signal, strongly depends on the bias values of the I and Q channels. On the other hand, from the perspective of Fourier transform, the bias values of the I and Q channels only affect the magnitude at the zero frequency. Therefore, narrowband RFI at zero frequency is unreliable.

Fig. 16 presents the mean results on a global scale. There is clearly a higher proportion of wideband RFI than narrowband RFI. Frequencies with high proportions of wideband RFI generally also have high proportions of narrowband RFI. The spike at zero frequency in the narrowband result is caused by the errors in I and Q biases. The frequency bands of 1266–1268 MHz and 1271–1274 MHz are less affected by RFI (The center frequency of ALOS-1 PALSAR is 1270 MHz, corresponding to the zero frequency in the figure).

Fig. 17 shows the regional scale results for Alaska, the continental United States, and mainland China. The manifestation of RFI varies across different regions due to the differences of RFI sources. As discussed in Section 4.1, the primary source of RFI in the continental United States is ARSR-4, while the RFI in northern Alaska primarily originates from NWS. In Alaska and the continental United States, the predominant form of interference is wideband RFI. In contrast, apart from wideband RFI, there is also notable narrowband RFI around the frequencies of 1264 MHz and 1274 MHz in China.

We further perform a more detailed spatial-frequency analysis by

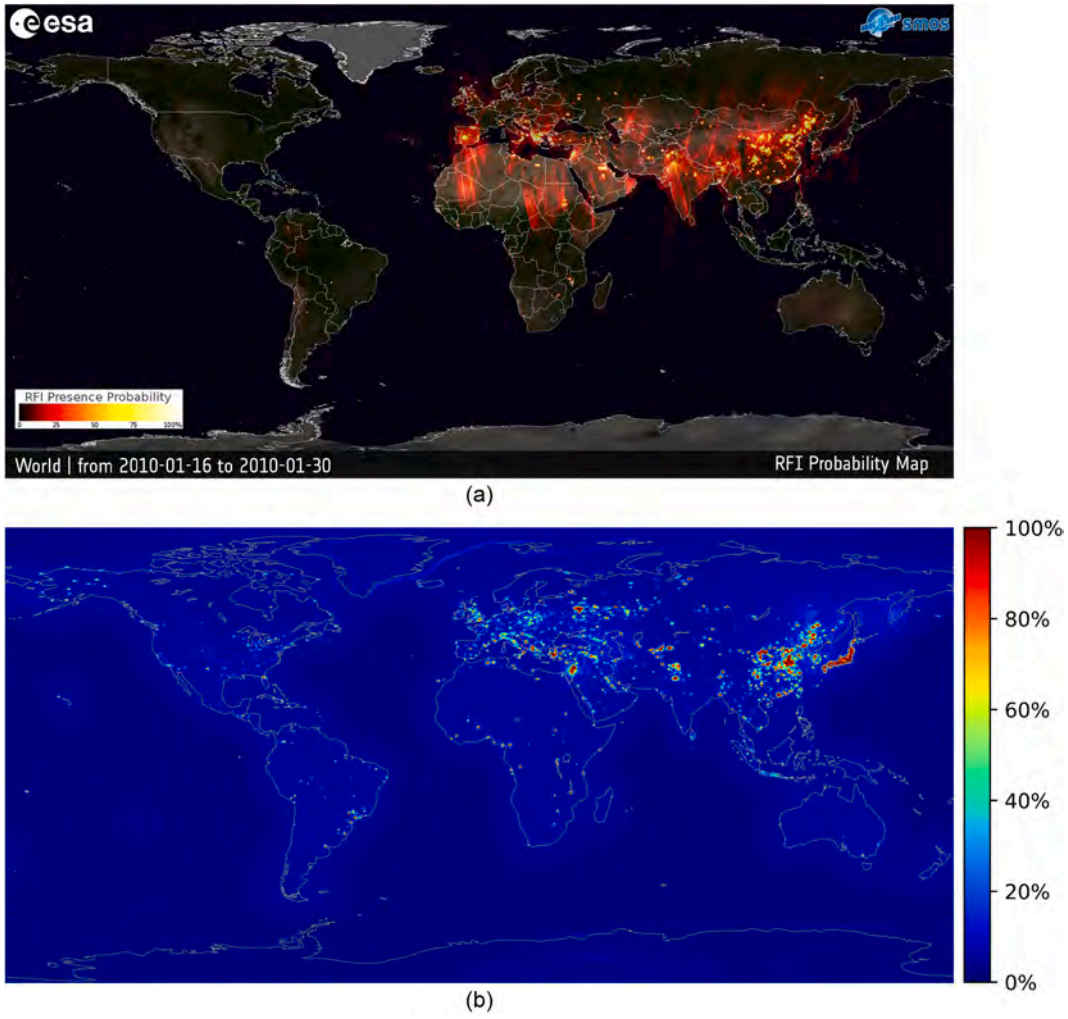

Fig. 15. Global distribution map of RFI from L-band passive microwave remote sensing missions. (a) RFI presence probability of SMOS from 2010 to 01–16 to 2010-01-30 retrieved from ESA RFI Monitoring & Information Tool (Uranga et al., 2022) at https://rfi.smos.eo.esa.int/rfimanager/publicindex.jsp. (b) SMAP RFI percentage in April 2015 retrieved from https://salinity.oceansciences.org/smap-radiometer.htm.

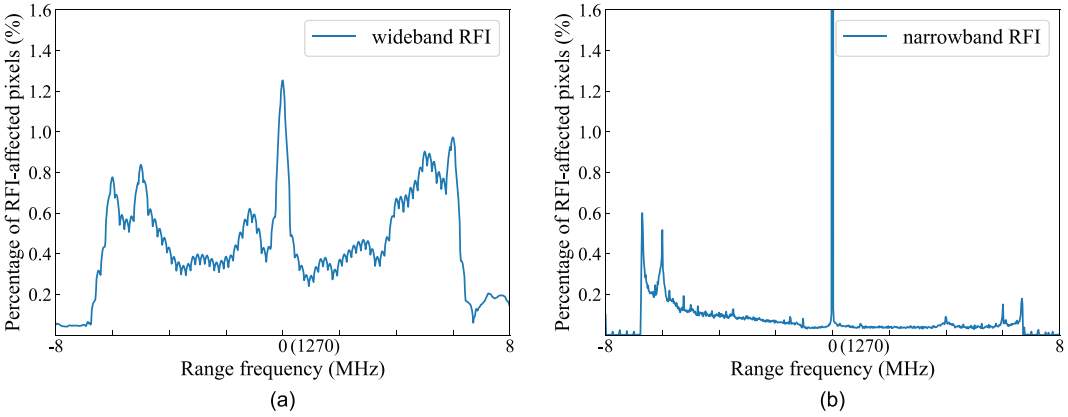

Fig. 16. Variations of global mean RFI impact (percentage of RFI-affected pixels) with frequency.

taking North America as an example. We focus on four frequency bands: 1260–1265 MHz, 1265–1270 MHz, 1270–1275 MHz, and 1275–1280 MHz, which aligns with the 5 MHz band intervals used in the United States Federal Government Spectrum Use Reports (National Telecommunications and Information Administration, 2024) for displaying spectrum contours for radars. The results are shown in Fig. 18. The NWS along the northern border of Alaska and Canada leads to consistent total RFI intensity across the frequency bands, but has minimal impacts on frequencies below 1265 MHz, in agreement with the Alaskan regional results shown in Fig. 17(a). In contrast, the total RFI intensity in the continental United States varies significantly across different frequency bands, especially in the northwestern and southern regions (highlighted

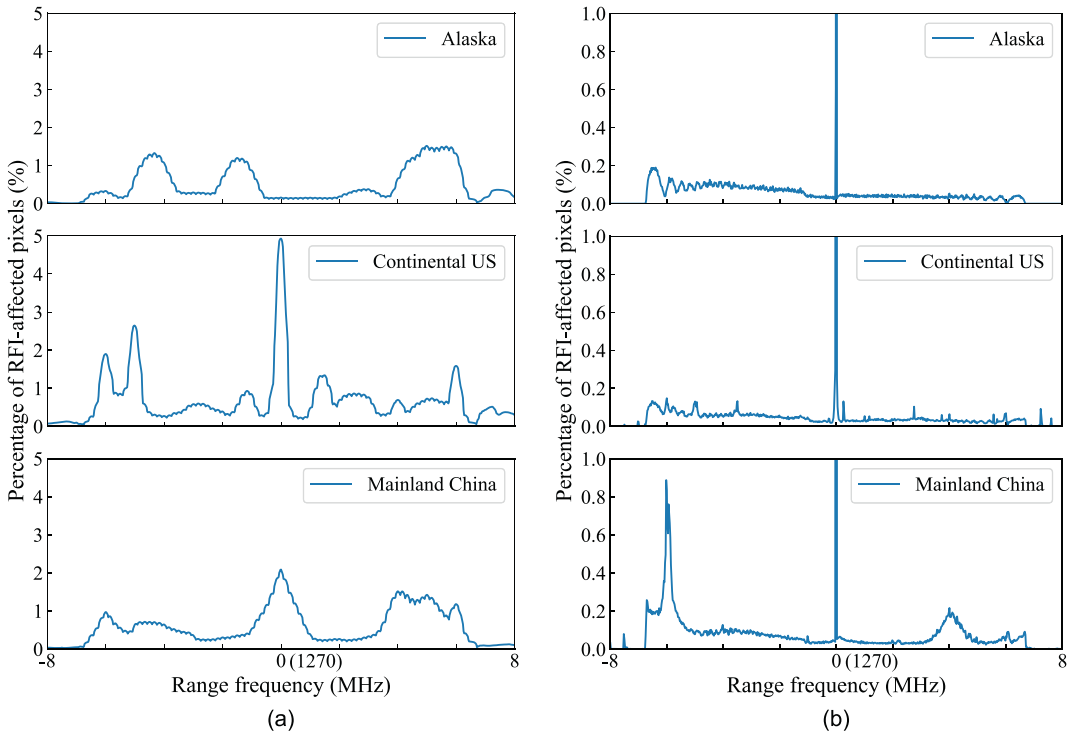

Fig. 17. Variations of mean RFI impact (the percentage of RFI-affected pixels) with frequency in Alaska, the continental United States, and mainland China. (a) Wideband RFI. (b) Narrowband RFI.

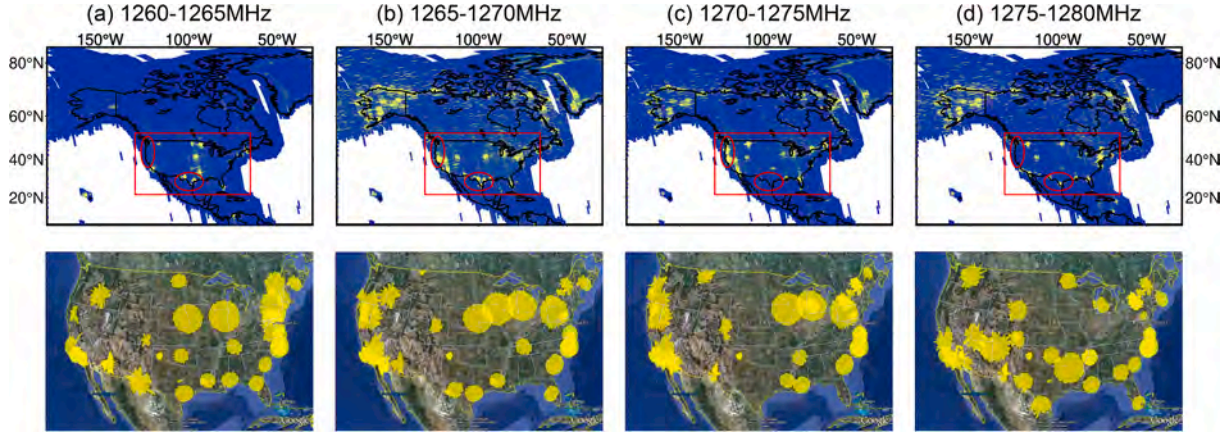

Fig. 18. Upper row: total RFI intensity across different frequency bands in North America. Lower row: spectrum contours for radars in the United States Federal Government Spectrum Compendium (National Telecommunications and Information Administration, 2024), including aeronautical radio-navigation and radio-location services. The contours indicate the locations where the radar signal power increases the thermal noise power of a generic ground-based communication receiver by 1 dB.

by the red ellipses in Fig. 18). This indicates the variations in the operating frequency bands of ARSR-4 sites, although other RFI sources might also be involved. Furthermore, the RFI results from different frequency bands are in agreement with the spectrum contours, indicating that the RFI record files we generated and the defined total RFI intensity can effectively and accurately reconstruct the sources of ground-based RFI.

4.6. Variations with time

Fig. 19 presents the global distribution of total RFI intensity from 2007 to 2010, measured with ALOS-1 FBD HH polarization data. In general, the regions experiencing severe RFI are consistent in different years, albeit with some subtle variations.

We also compute the temporal variance of the total RFI intensity from ALOS-1 FBD data in HH polarization as shown in Fig. 20. The distribution of RFI variance is consistent with the distribution of RFI itself. The large variance observed in China and Eastern Russia may suggest the increasing interference in these regions.

4.7. Correlation with population density

Since RFI is generated by human activities, there should be a correlation between RFI intensity and population density. Zhou et al. (2019) demonstrated a strong positive correlation between SMAP-derived RFI and population density across Chinese urban agglomerations. Fig. 21(a) shows the LandScan 2010 global population density with 1 km spatial resolution (Bright et al., 2011). Compared with Fig. 8

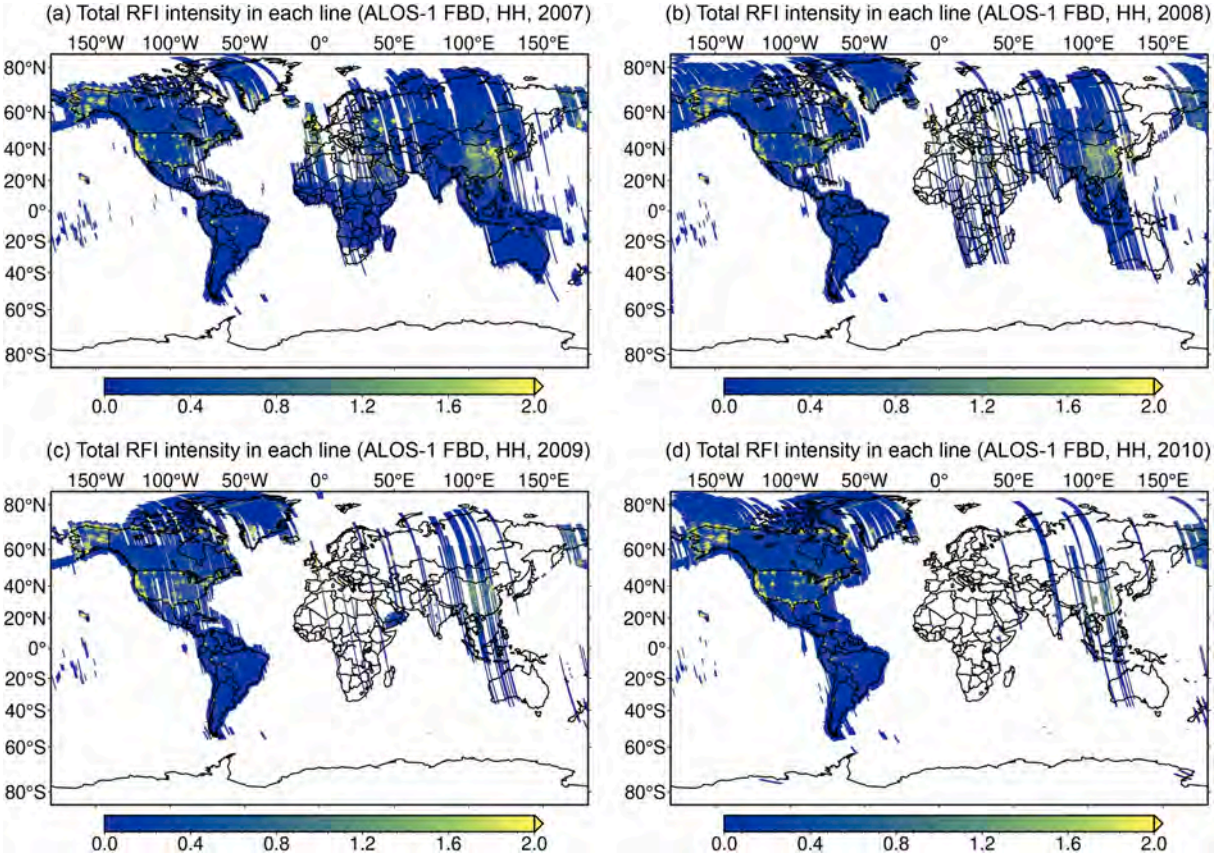

Fig. 19. Comparison of RFI distribution in different years.

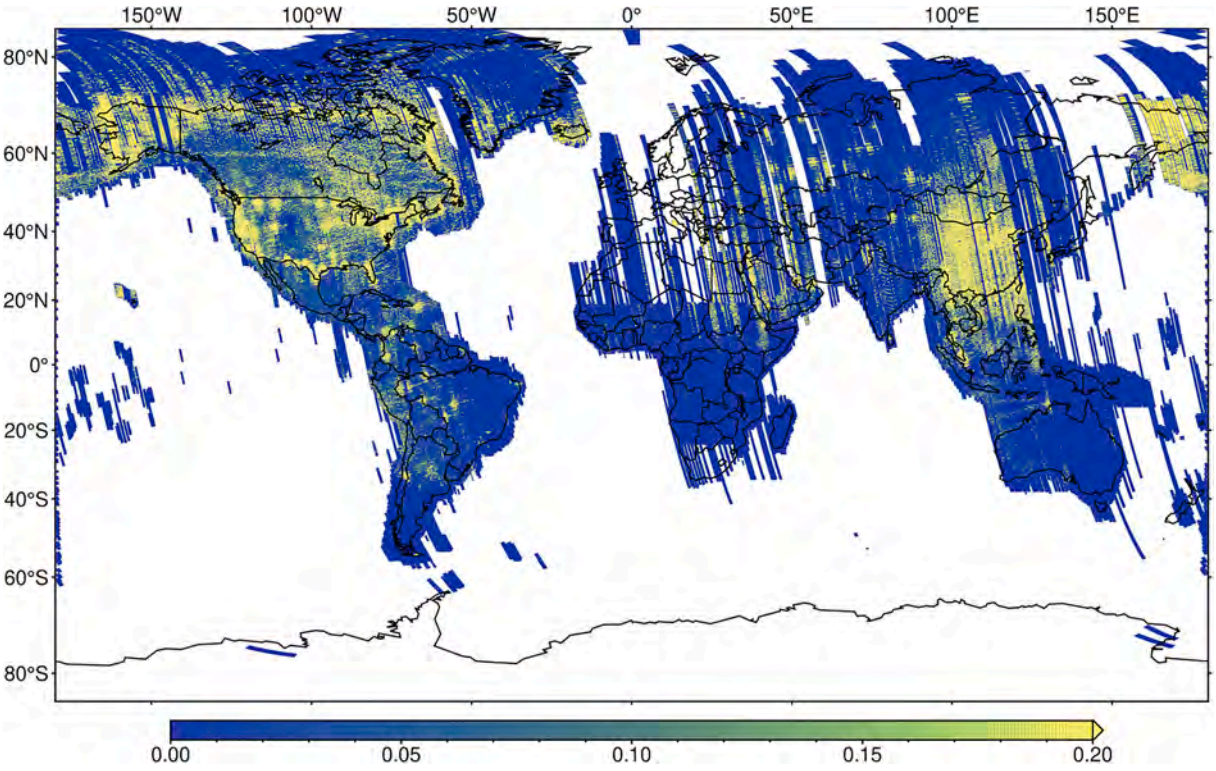

Fig. 20. The temporal variance of the total RFI intensity.

(a), however, high population density regions in Africa and India display minimal RFI. In North America, the overwhelming RFI contributions from NWS and ARSR-4 systems obscure any population density correlation. Meanwhile, the RFI data for Europe derived from ALOS-1 raw data are incomplete. Therefore, we analyze the correlation between RFI intensity and population density in China. Furthermore, we use total RFI intensity in each line for the correlation analysis.

Considering the spatial resolution of the detected RFI and the ambiguities in locating the detected RFI, we use a grid size of 800 km × 800 km for the correlation analysis as shown in Fig. 21(b). A linear regression between mean population density and mean RFI intensity yields a correlation coefficient of 0.71 as shown in Fig. 21(c).

5. Implications

The results from this study provide implications for a variety of aspects. Here we discuss some of them. The already severe RFI pollution and its increasing trend raise the strong need of regulations at international and national levels to reduce RFI pollution for the microwave band allocated for active remote sensing (National Academies of Sciences, Engineering, and Medicine, 2015). This involves the effort of not only science community, but also government and industry. Such effort has proved to be successful in dramatically reducing RFI in passive remote sensing.

For the design of future L-band SAR missions, RFI should also be taken into account. For example, reducing the impacts of RFI requires the radar transmit power should be raised so that the received radar signal is much stronger than RFI signals. The SweepSAR technique (Freeman et al., 2009) used by NISAR (Kellogg et al., 2020) requires a transmit power several times lower than regular SAR. This pro unfortunately turns out to be a con as far as RFI is concerned. Some SAR systems, such as NISAR and ALOS-4, add a side band for InSAR ionospheric correction. This side band might be completely corrupted by RFI. For making global observation plans for SAR systems with a limited duty cycle, the global RFI maps can guide the use of the limited duty cycle.

The end data users should also pay attention to the RFI issue depending on study area and application. The global RFI maps directly provide information about the RFI levels for different areas. The most commonly used RFI mitigation algorithm is notch filtering, and the impacts of the resulting loss of range spectrum should be evaluated for specific applications. Furthermore, as cross-polarization data are more susceptible to RFI, polarization applications are affected.

6. Conclusions

We have developed algorithms, workflow and system for operationally measuring RFI. We have defined an RFI format that can be easily used to compute a number of RFI metrics, in particular, the total RFI intensity, which proves to be very useful. We processed all the archived ALOS-1 and JERS-1 data that are publicly available, generating global RFI maps. We find

(1) The spatial distribution of RFI shows that heavy RFI pollutions are mainly in three regions: East Asia, North America, and the region consisting of Europe, North Africa and the Middle East. The RFI sources are different in different regions.
(2) It is challenging to measure RFI in Greenland and Antarctica because of the unique radar backscatter of the snow and ice in these regions.
(3) Comparison of results from different polarizations shows that cross polarization data are more susceptible to RFI, since their radar backscatter is lower.
(4) Comparison of results from ALOS-1 and JERS-1 indicates the increasing trend of RFI pollution.
(5) Comparison with C-band Envisat result shows that RFI at L-band is significantly more severe than at C-band, in agreement with previous observations.
(6) The global RFI distribution from L-band SAR data is similar to that from L-band passive radiometers including SMOS and SMAP.

We also analyzed the variations of RFI with region, frequency and time, as well as the correlation with population density. The results provide references for satellite mission design and operation, systematic mitigation of RFI, improving the management of electromagnetic spectrum, etc. This becomes more important as we are entering the golden age of L-band satellite SAR missions.

CRediT authorship contribution statement

Yuhang Wang: Writing – review & editing, Writing – original draft, Visualization, Validation, Software, Resources, Methodology, Investigation, Formal analysis, Data curation, Conceptualization. **Cunren Liang:** Writing – review & editing, Visualization, Validation, Supervision, Methodology, Investigation, Funding acquisition, Formal analysis, Data curation, Conceptualization. **Fan Yang:** Data curation. **Ligong**

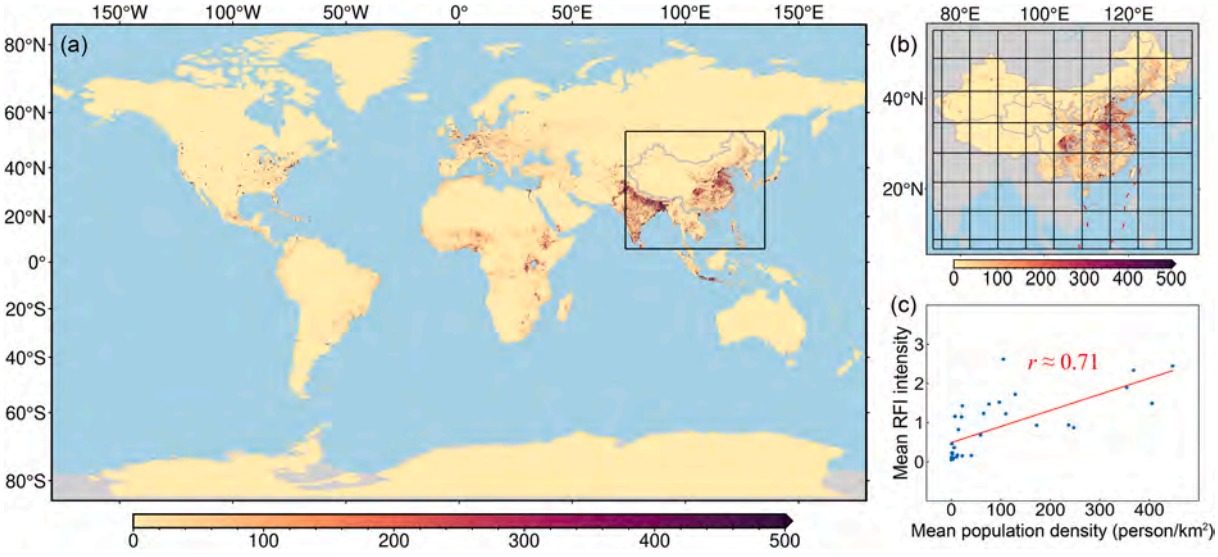

Fig. 21. Correlation of RFI intensity and population density. (a) Global population density from the LandScan Global 2010 dataset (Bright et al., 2011). (b) Grid size for the correlation analysis. (c) Linear regression result.

Yang: Data curation. **Shangzong Lu:** Data curation. **Xue Li:** Visualization. **Qiming Zeng:** Validation.

Declaration of competing interest

The authors declare that they have no known competing financial interests or personal relationships that could have appeared to influence the work reported in this paper.

Acknowledgements

This work was supported by National Natural Science Foundation of China under grant 42274026. We thank Japan Aerospace Exploration Agency (JAXA) and European Space Agency (ESA) for making ALOS-1, JERS-1 and Envisat SAR data available to us. ALOS-1 data were downloaded from Alaska Satellite Facility (ASF). We thank Yan Soldo, European Space Agency (ESA/ESTEC), Noordwijk, Netherlands, and Ekhi Uranga, Ingeniería de Sistemas para la Defensa de España (ISDEFE), Madrid, Spain, for discussions about RFI from SMOS. We thank the editors and reviewers for their comments on this paper.

Appendix A. RFI record format

Parameter	Format	Description
Block header		
Block number	Unsigned short	Starts from 1
Absolute orbit number	Unsigned short	
Number of bytes in block header	Unsigned int	128+12* N (N = Number of PRFs)
Transmitted polarization	Unsigned char	0=H, 1=V
Received polarization	Unsigned char	0=H, 1=V
Number of SAR data records	Unsigned int	Total number of lines of the block
Range sampling rate	Double	
Range bandwidth	Double	
FFT length	Unsigned short	FFT length for computing range spectrum
Start time	Customized time format	Unsigned short (year) + Unsigned char * 5 (month, day, hour, minute, second) + Unsigned int (milliseconds)
Corrected start time	Customized time format	
End Time	Customized time format	
Corrected end time	Customized time format	
Number of smaller blocks	Unsigned short	A block is divided into a number of smaller blocks according to starting ranges.
Doppler centroid coefficients	Double*6	Doppler centroid frequency = A + B*x + C*x*x + D*y + E*y*y + F*x*y, where x is the column number starting from 0, and y is the time span from the first line measured in seconds.
Number of PRFs	Unsigned short	
First PRF	Double	Repeats N times (N = number of PRFs)
Start line of first PRF	Unsigned int	
Smaller block header		
Smaller block number	Unsigned short	Starts from 1
Number of bytes of subblock header	Unsigned int	24+12*N (N = Number of standard frame files)
Number of lines in the smaller block	Unsigned int	
Number of columns in the smaller block	Unsigned short	
Starting range	Double	
Number of standard frames files used	Unsigned short	
First frame number	Unsigned int	Repeats N times (N = number of frames)
Start line of first frame	Unsigned int	
End line of first frame	Unsigned int	
Number of subblocks	Unsigned short	

Repeat N times (N = Number of smaller blocks)		
Subblock header		
Number of lines in the subblock	Unsigned short	
Number of valid lines in the subblock	Unsigned short	Introduced for JERS-1 data, not included in the ALOS-1 results, as JERS-1 data may contain many invalid lines.
Corrected start time	Customized time format	
Corrected end time	Customized time format	
First line position	Double*4	Minimum latitude, maximum latitude, minimum longitude, maximum longitude
End line position	Double*4	
Number of bytes used for recording RFI	Unsigned int	
RFI of each line		
Number of detected RFIs	Unsigned int	
Mean intensity of this line	Double	
RFI start frequency pixel index	Unsigned short	Repeats N times (N = Number of detected RFI)
RFI end frequency pixel index	Unsigned short	
Mean intensity of RFI	Double	
RFI of each column		
Number of detected RFIs	Unsigned int	
RFI start line index	Unsigned short	Repeats N times (N = Number of detected RFI)
RFI end line index	Unsigned short	
Mean intensity of RFI	Double	
Repeat N times (N = Number of subblocks)		

Block body = (smaller block header + smaller block body) * N, N = number of smaller blocks.
Smaller block body = (subblock header + RFI) * N, N = number of subblocks.

Appendix B. Unit of total RFI intensity

The total intensity of RFI is computed by summing the squared magnitude of all RFI-affected pixels in each line in the range frequency domain. The range frequency spectrum is computed by the Fourier transform of raw data. The absolute unit of total RFI intensity thus depends on the absolute unit of the raw data.

The generation of raw data involves a number of processes with parameters not known to us, such as the factor for converting electric field strength to voltage, the gain of the low noise amplifier, and the scaling factor for mapping sampled signals to raw data (e.g. 8-bit unsigned integer values). In fact, these parameters are normally not disclosed.

Another method starts from the radar equation

$$P_r = \frac{P_t G^2 \sigma}{(4\pi)^3 R^4 \lambda^2 L} \tag{B.1}$$

where P_r is the received power, P_t is the transmitted power, G is the antenna gains, σ is the radar cross section, R is the slant range, λ is the radar wavelength, and L is the loss factor. $L = L_{\text{atmos}} \bullet L_{\text{radar}}$, where L_{atmos} is the atmospheric loss factor during the wave propagation, and L_{radar} is the microwave transmission loss factor due to miscellaneous sources (Doerry, 2006). The loss factor can be estimated in the calibration process (Crisp, 2018).

The radar cross section σ can be computed by

$$\sigma = \sigma^0 \frac{\beta R}{\sin\theta} \frac{C\tau}{2} \tag{B.2}$$

where σ^0 is the normalized radar cross section (NRCS), β is the azimuth antenna beam width, R is the slant range, θ is the incident angle, C is the speed of light, and τ is the pulse width. The parameters are normally made available for converting SLC or raw data to σ^0. However, the loss factor is not known to us.

In conclusion, we are not able to determine the absolute physical unit of raw data, since some associated radar system parameters are not available to us.

According to Eq. (B.1), the received signal power primarily depends on the transmitted power, wavelength, and backscatter coefficient. This explains not only the higher percentage of RFI-affected pixels in JERS-1 data compared to ALOS-1, but also elucidates both the more severe RFI in HV polarization than in HH polarization observed in ALOS-1 FBD mode data and the higher RFI occurrence over ocean surfaces.

Appendix C. Supplementary data

Supplementary data to this article can be found online at https://doi.org/10.1016/j.rse.2025.114955.

Data availability

Data will be made available on request.

References

Andrews, M.J., Johnson, J.T., Brogioni, M., Macelloni, G., Jezek, K.C., 2021. Properties of the 500–2000-MHz RFI environment observed in high-latitude airborne radiometer measurements. IEEE Trans. Geosci. Remote Sens. 60, 1–11. https://doi.org/10.1109/TGRS.2021.3090945.

Arai, H., Le Toan, T., Takeuchi, W., Oyoshi, K., Fumoto, T., Inubushi, K., 2022. Evaluating irrigation status in the Mekong Delta through polarimetric L-band SAR data assimilation. Remote Sens. Environ. 279, 113139. https://doi.org/10.1016/j.rse.2022.113139.

Artiemjew, P., Chojka, A., Rapiński, J., 2020. Deep learning for RFI artifact recognition in Sentinel-1 data. Remote Sens 13, 7. https://doi.org/10.3390/rs13010007.

Ashcraft, I.S., Long, D.G., 2005. Observation and characterization of radar backscatter over Greenland. IEEE Trans. Geosci. Remote Sens. 43, 225–237. https://doi.org/10.1109/TGRS.2004.841484.

Benson, Carl S., 1960. Stratigraphic Studies in the Snow and Firn of the Greenland Ice Sheet. Dissertation (Ph.D.). California Institute of Technology. https://doi.org/10.7907/G7V2-0T57.

Bright, E., Coleman, P., Rose, A., Urban, M., 2011. LandScan Global 2010 [Data Set]. Oak Ridge National Laboratory. https://doi.org/10.48690/1524206.

Bringer, A., Daehn, M., Johnson, J.T., Soldo, Y., Le Vine, D.M., de Pedro, P., Piepmeier, J. R., Mohammed, P., 2018. SMAP mission: changes in the RFI environment. In: 2018 IEEE International Geoscience and Remote Sensing Symposium, pp. 3754–3757. https://doi.org/10.1109/IGARSS.2018.8519067.

Buckreuss, S., Horn, R., 1998. E-SAR P-band SAR subsystem design and RF-interference suppression. In: 1998 IEEE International Geoscience and Remote Sensing Symposium, 1, pp. 466–468. https://doi.org/10.1109/IGARSS.1998.702941.

Chan, S., Fischman, M., Spencer, M., 2011. RFI mitigation and detection for the SMAP radar. In: 2011 IEEE International Geoscience and Remote Sensing Symposium, pp. 2725–2728. https://doi.org/10.1109/IGARSS.2011.6049777.

Chang, Q., Zwieback, S., DeVries, B., Berg, A., 2022. Application of L-band SAR for mapping tundra shrub biomass, leaf area index, and rainfall interception. Remote Sens. Environ. 268, 112747. https://doi.org/10.1016/j.rse.2021.112747.

Chen, D., Yang, J., Wu, J., Tang, H., Huang, M., 2012. Spectrum occupancy analysis based on radio monitoring network. In: 2012 1st IEEE International Conference on Communications in China (ICCC), pp. 739–744. https://doi.org/10.1109/ICCChina.2012.6356981.

Chen, J., Tao, M., Liu, Y., Li, T., Liu, Y., Li, J., Tang, C., Li, J., Wang, L., 2024. Characterization and mitigation of radio frequency interference signatures in L-band LuTan-1 InSAR system: first results and assessment. IEEE Trans. Radar Syst. 2, 404–420. https://doi.org/10.1109/TRS.2024.3385181.

Chiang, R.I., Rowe, G.B., Sowerby, K.W., 2007. A quantitative analysis of spectral occupancy measurements for cognitive radio. In: 2007 IEEE 65th Vehicular Technology Conference-VTC2007-Spring, pp. 3016–3020. https://doi.org/10.1109/VETECS.2007.618.

Crisp, D.J., 2018. Robust absolute calibration for SAR. In: 2018 International Conference on Radar, pp. 1–6. https://doi.org/10.1109/RADAR.2018.8557317.

De Matthaeis, P., Oliva, R., Soldo, Y., Cruz-Pol, S., 2018. Spectrum management and its importance for microwave remote sensing. IEEE Geosci. Remote Sens. Mag. 6, 17–25. https://doi.org/10.1109/MGRS.2018.2832057.

Doerry, A.W., 2006. Performance Limits for Synthetic Aperture Radar, Second edition, p. 70. Sandia Report SAND2006-0821.

Federal Aviation Administration, US Air Force, 2002. ARSR-4 (FPS-130). https://www.forecastinternational.com/archive/disp_pdf.cfm?DACH_RECNO=739.

Fraser, A.D., Young, N.W., Adams, N., 2013. Comparison of microwave backscatter anisotropy parameterizations of the Antarctica ice sheet using ASCAT. IEEE Trans. Geosci. Remote Sens. 52, 1583–1595. https://doi.org/10.1109/TGRS.2013.2252621.

Fraser, A.D., Nigro, M.A., Ligtenberg, S.R., Legresy, B., Inoue, M., Cassano, J.J., Munneke, P.K., Lenaerts, J.T.M., Young, N.W., Treverrow, A., Broeke, M.V.D., Enomoto, H., 2016. Drivers of ASCAT C band backscatter variability in the dry snow zone of Antarctica. J. Glaciol. 62, 170–184. https://doi.org/10.1017/jog.2016.29.

Freeman, A., Saatchi, S.S., 2004. On the detection of Faraday rotation in linearly polarized L-band SAR backscatter signatures. IEEE Trans. Geosci. Remote Sens. 42, 1607–1616. https://doi.org/10.1109/TGRS.2004.830163.

Freeman, A., Krieger, G., Rosen, P., Younis, M., Johnson, W.T., Huber, S., Jordan, R., Moreira, A., 2009. SweepSAR: beam-forming on receive using a reflector-phased array feed combination for spaceborne SAR. In: 2009 IEEE Radar Conference, pp. 1–9. https://doi.org/10.1109/RADAR.2009.4977140.

Grimaldi, S., Xu, J., Li, Y., Pauwels, V.R., Walker, J.P., 2020. Flood mapping under vegetation using single SAR acquisitions. Remote Sens. Environ. 237, 111582. https://doi.org/10.1016/j.rse.2019.111582.

Haghighi, M.H., Motagh, M., 2019. Ground surface response to continuous compaction of aquifer system in Tehran, Iran: results from a long-term multi-sensor InSAR analysis. Remote Sens. Environ. 221, 534–550. https://doi.org/10.1016/j.rse.2018.11.003.

Healy, T.A., McDonald, R.K., Pomrink, R.F., Conklin, W.P., 1997. Air Route Surveillance Radar Model 4 (ARSR-4) Operational Test and Evaluation (OT&E) Final Report. Federal Aviation Administration Technical Center, Atlantic City, NJ, USA. https://apps.dtic.mil/sti/tr/pdf/ADA327689.pdf.

Huang, X., Liang, D., 1999. Gradual RELAX algorithm for RFI suppression in UWB-SAR. Electron. Lett. 35, 1916–1917. https://api.semanticscholar.org/CorpusID:111013004.

Japan Aerospace Exploration Agency, Earth Observation Research Center. ALOS data users handbook (Revision C). https://www.eorc.jaxa.jp/ALOS/en/doc/fdata/ALOS_HB_RevC_EN.pdf.

Kaihotsu, I., Imaoka, K., Fujii, H., Oyunbaatar, D., Yamanaka, T., Shiraishi, K., Koike, T., 2013. First evaluation of SMOS L2 soil moisture products using in situ observation data of MAVEX on the Mongolian Plateau in 2010 and 2011. Hydrol. Res. Lett. 7, 30–35. https://doi.org/10.3178/hrl.7.30.

Kellogg, K., Hoffman, P., Standley, S., Shaffer, S., Rosen, P., Edelstein, W., Dunn, C., Baker, C., Barela, P., Shen, Y., Guerrero, A.M., Xaypraseuth, P., Sagi, V.R., Sreekantha, C.V., Harinath, N., Kumar, R., Bhan, R., Sarma, C.V.H.S., 2020. NASA-ISRO synthetic aperture radar (NISAR) mission. In: 2020 IEEE Aerospace Conference, pp. 1–21. https://doi.org/10.1109/AERO47225.2020.9172638.

Lackenbauer, P.W., Farish, M.J., Arthur-Lackenbauer, J., 2005. The Distant Early Warning (DEW) Line. Arctic Institute of North America. https://pubs.aina.ucalgary.ca/aina/DEWLineBib.pdf.

Li, N., Lv, Z., Guo, Z., Zhao, J., 2021. Time-domain notch filtering method for pulse RFI mitigation in synthetic aperture radar. IEEE Geosci. Remote Sens. Lett. 19, 1–5. https://doi.org/10.1109/LGRS.2021.3077247.

Li, N., Lv, Z., Guo, Z., 2022. Pulse RFI mitigation in synthetic aperture radar data via a three-step approach: location, notch, and recovery. IEEE Trans. Geosci. Remote Sens. 60, 1–17. https://doi.org/10.1109/TGRS.2022.3161368.

Liang, C., Fielding, E.J., Liu, Z., Motohka, T., Natsuaki, R., Yun, S.H., 2024. An analysis of the potentials of L-band SAR satellites for measuring azimuth motion. Remote Sens. Environ. 315, 114426. https://doi.org/10.1016/j.rse.2024.114426.

Liu, Z., Liao, G., Yang, Z., 2013. Time variant RFI suppression for SAR using iterative adaptive approach. IEEE Geosci. Remote Sens. Lett. 10, 1424–1428. https://doi.org/10.1109/LGRS.2013.2259575.

Liu, H., Li, D., Zhou, Y., Truong, T.K., 2018. Simultaneous radio frequency and wideband interference suppression in SAR signals via sparsity exploitation in time–frequency domain. IEEE Trans. Geosci. Remote Sens. 56, 5780–5793. https://doi.org/10.1109/TGRS.2018.2825459.

Liu, X., Zhao, C., Zhang, Q., Yin, Y., Lu, Z., Samsonov, S., Yang, C., Wang, M., Tomás, R., 2021. Three-dimensional and long-term landslide displacement estimation by fusing C-and L-band SAR observations: a case study in Gongjue County, Tibet, China. Remote Sens. Environ. 267, 112745. https://doi.org/10.1016/j.rse.2021.112745.

Lu, X., Yang, J., Yeo, T.S., Su, W., Gu, H., Yu, W., 2021. Accurate SAR image recovery from RFI contaminated raw data by using image domain mixed regularizations. IEEE Trans. Geosci. Remote Sens. 60, 1–13. https://doi.org/10.1109/TGRS.2021.3097977.

Lyu, Q., Han, B., Li, G., Sun, W., Pan, Z., Hong, W., Hu, Y., 2021. SAR interference suppression algorithm based on low-rank and sparse matrix decomposition in time–frequency domain. IEEE Geosci. Remote Sens. 19, 1–5. https://doi.org/10.1109/LGRS.2020.3048161.

Madsen, S.N., 1989. Estimating the Doppler centroid of SAR data. IEEE Trans. Aerosp. Electron. Syst. 25, 134–140. https://doi.org/10.1109/7.18675.

Mao, Y., Huang, Y., Yu, X., Chen, X., Zhang, Z., Chen, Z., Hong, W., 2024. A novel group-parametric model for RFI suppression on spaceborne SAR. IEEE Trans. Geosci. Remote Sens. 63, 1–14. https://doi.org/10.1109/TGRS.2024.3508254.

Meyer, F.J., Nicoll, J.B., Doulgeris, A.P., 2011. Investigations on Radio Frequency Interference Signatures in ALOS PALSAR Data. CEOS SAR Cal/Val 2011. Fairbanks. https://calvalportal.ceos.org/html/portal/sarc/documents/documents/Investigations_on_Radio_Frequency_Interference_Signatures_J.Nicoll.pdf.

Meyer, F.J., Nicoll, J.B., Doulgeris, A.P., 2013. Correction and characterization of radio frequency interference signatures in L-band synthetic aperture radar data. IEEE Trans. Geosci. Remote Sens. 51, 4961–4972. https://doi.org/10.1109/TGRS.2013.2252469.

Miller, T.R., McCorkle, J.W., Potter, L.C., 1995. Near-least-squares radio frequency interference suppression. In: Algorithms for Synthetic Aperture Radar Imagery II, 2487, pp. 72–83.

Mohammed, P.N., Aksoy, M., Piepmeier, J.R., Johnson, J.T., Bringer, A., 2016. SMAP L-band microwave radiometer: RFI mitigation prelaunch analysis and first year on-orbit observations. IEEE Trans. Geosci. Remote Sens. 54, 6035–6047. https://doi.org/10.1109/TGRS.2016.2580459.

National Academies of Sciences, Engineering, and Medicine, 2015. A Strategy for Active Remote Sensing Amid Increased Demand for Radio Spectrum. The National Academies Press, Washington, DC. https://doi.org/10.17226/21729.

National Research Council, 2010. Spectrum Management for Science in the 21st Century. The National Academies Press, Washington, DC. https://doi.org/10.17226/12800.

National Telecommunications and Information Administration, 2024. Federal Government Spectrum Use Reports 225 MHz – 7.125 GHz. https://www.ntia.gov/files/ntia/publications/compendium/1240.00-1300.00_01DEC15.pdf (accessed 18 December 2024).

Nguyen, L.H., Tran, T.D., 2016. Efficient and robust RFI extraction via sparse recovery. IEEE J. Sel. Top. Appl. Earth Obs. Remote Sens. 9, 2104–2117. https://doi.org/10.1109/JSTARS.2016.2528884.

Njoku, E.G., Ashcroft, P., Chan, T.K., Li, L., 2005. Global survey and statistics of radio-frequency interference in AMSR-E land observations. IEEE Trans. Geosci. Remote Sens. 43 (5), 938–947. https://doi.org/10.1109/TGRS.2004.837507.

Oliva, R., Daganzo, E., Richaume, P., Kerr, Y., Cabot, F., Soldo, Y., Anterrieu, E., Reul, N., Gutierrez, A., Barbosa, J., Lopes, G., 2016. Status of radio frequency interference (RFI) in the 1400–1427 MHz passive band based on six years of SMOS mission. Remote Sens. Environ. 180, 64–75. https://doi.org/10.1016/j.rse.2016.01.013.

Parinussa, R.M., Holmes, T.R., Wanders, N., Dorigo, W.A., de Jeu, R.A., 2015. A preliminary study toward consistent soil moisture from AMSR2. J. Hydrometeorol. 16, 932–947. https://doi.org/10.1175/JHM-D-13-0200.1.

Patil, K., Skouby, K., Chandra, A., Prasad, R., 2011. Spectrum occupancy statistics in the context of cognitive radio. In: 2011 the 14th International Symposium on Wireless Personal Multimedia Communications (WPMC), pp. 1–5.

Pedro, L., Sá, M., Fernandes, R., Jorge, F., Mendonça, S., 2022. Protection of Earth observation satellites from radio-frequency interference: policies and practices [perspectives]. IEEE Geosci. Remote Sens. Mag. 10, 278–288. https://doi.org/10.1109/MGRS.2022.3221824.

Rosen, P.A., Gurrola, E., Sacco, G.F., Zebker, H., 2012. The InSAR scientific computing environment. In: 9th European Conference on Synthetic Aperture Radar, pp. 730–733.

Shimada, M., 2005. L-band radio interferences observed by the JERS-1 SAR and its global distribution. In: 2005 IEEE International Geoscience and Remote Sensing Symposium, pp. 2752–2755. https://doi.org/10.1109/IGARSS.2005.1525637.

Shimada, M., Isoguchi, O., Tadono, T., Higuchi, R., Isono, K., 2007. PALSAR CALVAL summary and update 2007. In: 2007 IEEE International Geoscience and Remote Sensing Symposium, pp. 3593–3596. https://api.semanticscholar.org/CorpusID:12117370.

Shimada, M., Itoh, T., Motooka, T., Watanabe, M., Shiraishi, T., Thapa, R., Lucas, R., 2014. New global forest/non-forest maps from ALOS PALSAR data (2007–2010). Remote Sens. Environ. 155, 13–31. https://doi.org/10.1016/j.rse.2014.04.014.

Sorensen, K.A., Kusk, A., Heiselberg, P., Heiselberg, H., 2023. Finding ground-based radars in SAR images: localizing radio frequency interference using unsupervised deep learning. IEEE Trans. Geosci. Remote Sens. 61, 1–15. https://doi.org/10.1109/TGRS.2023.3295002.

Spencer, M., Ulaby, F., 2016. Spectrum issues faced by active remote sensing: radio frequency interference and operational restrictions technical committees. IEEE Geosci. Remote Sens. Mag. 4, 40–45. https://doi.org/10.1109/MGRS.2016.2517410.

Spencer, M.W., Chen, C.W., Ghaemi, H., Chan, S.F., Belz, J.E., 2013. RFI characterization and mitigation for the SMAP radar. IEEE Trans. Geosci. Remote Sens. 51, 4973–4982. https://doi.org/10.1109/TGRS.2013.2253472.

Su, J., Xi, M., Gong, Y., Tao, M., Fan, Y., Wang, L., 2022. Time-varying wideband interference mitigation for SAR via time-frequency-pulse joint decomposition algorithm. IEEE Trans. Geosci. Remote Sens. 60, 1–16. https://doi.org/10.1109/TGRS.2022.3213318.

Tao, M., Su, J., Huang, Y., Wang, L., 2019. Mitigation of radio frequency interference in synthetic aperture radar data: current status and future trends. Remote Sens 11, 2438. https://doi.org/10.3390/rs11202438.

Tao, M., Li, J., Su, J., Wang, L., 2022. Characterization and removal of RFI artifacts in radar data via model-constrained deep learning approach. Remote Sens 14, 1578. https://doi.org/10.3390/rs14071578.

Uranga, E., Llorente, Á., de la Fuente, A., 2018. Database of SMOS RFI sources in the 1400-1427MHZ passive band. In: 2018 IEEE Global Conference on Signal and Information Processing, pp. 1095–1098. https://doi.org/10.1109/GlobalSIP.2018.8646378.

Uranga, E., Llorente, Á., González, J., de la Fuente, A., Oliva, R., Soldo, Y., Jorge, F., 2022. SMOS ESA RFI monitoring and information tool: lessons learned. Remote Sens 14, 5387. https://doi.org/10.3390/rs14215387.

Wikipedia contributors, 2024a. Joint Surveillance System. https://en.wikipedia.org/wiki/Joint_Surveillance_System (accessed 18 December, 2024).

Wikipedia contributors, 2024b. North Warning System. https://en.wikipedia.org/wiki/North_Warning_System (accessed 18 December, 2024).

Wildemeersch, M., Fortuny-Guasch, J., 2010. Radio frequency interference impact assessment on global navigation satellite systems. In: EC Joint Research Centre, Security Tech. Assessment Unit, Tech. Rep, pp. 50–51.

Xu, W., Xing, W., Fang, C., Huang, P., Tan, W., 2020. RFI suppression based on linear prediction in synthetic aperture radar data. IEEE Geosci. Remote Sens. Lett. 18, 2127–2131. https://doi.org/10.1109/LGRS.2020.3015205.

Yang, H., Li, K., Li, J., Du, Y., Yang, J., 2021. BSF: block subspace filter for removing narrowband and wideband radio interference artifacts in single-look complex SAR images. IEEE Trans. Geosci. Remote Sens. 60, 1–16. https://doi.org/10.1109/TGRS.2021.3096538.

Zhao, J., Zou, X., Weng, F., 2013. WindSat radio-frequency interference signature and its identification over Greenland and Antarctic. IEEE Trans. Geosci. Remote Sens. 51, 4830–4839. https://doi.org/10.1109/TGRS.2012.2230634.

Zhou, F., Tao, M., Bai, X., Liu, J., 2013. Narrow-band interference suppression for SAR based on independent component analysis. IEEE Trans. Geosci. Remote Sens. 51, 4952–4960. https://doi.org/10.1109/TGRS.2013.2244605.

Zhou, W.C., Han, Z., Han, S.Y., Wang, Y.Q., Zhang, X.W., Wu, Y.S., 2019. Characteristics of L-band radio frequency interference detected via the soil moisture active passive radiometer in China and its offshore areas. Results Phys 12, 1859–1865. https://doi.org/10.1016/j.rinp.2019.01.062.

Supplementary Information

Global radio frequency interference in L-band SAR data from ALOS-1 and JERS-1 satellites

Yuhang Wang, Cunren Liang, Fan Yang, Ligong Yang, Shangzong Lu, Xue Li, Qiming Zeng

Correspondence to cunren.liang@pku.edu.cn

Structure and Content of the Supplementary Information

Figure S1: Range spectra before and after the removal of Gibbs phenomenon (fixed I/Q bias).

Figure S2: Range spectra before and after the removal of Gibbs phenomenon (adaptive I/Q bias).

Figure S3: The improvement of cluster analysis on RFI detection results.

Figure S4: The improvement of morphological processing on RFI detection results.

Figure S5: Reconstruction of range spectrum from RFI record file.

Figure S6: Single-Look Complex (SLC) images before and after RFI mitigation.

Figure S7: Abnormal starting range and PRF values in JERS-1 raw data.

Figure S8: Abnormal radar echoes in JERS-1 raw data.

Figure S9: Envisat ASAR SLC images before and after azimuth defocusing.

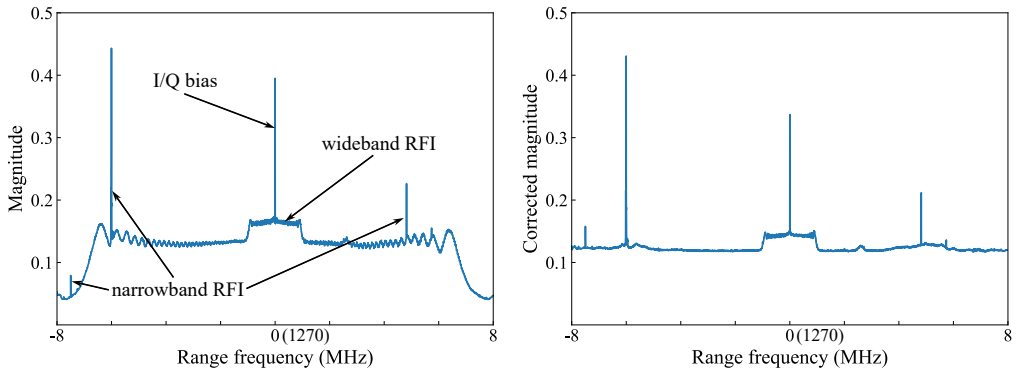

(a) (b)

Figure S1. Range spectra before (a) and after (b) removing spectrum magnitude fluctuations for a scene that is acquired by ALOS-1 in FBD mode (ALPSRP145510770-L1.0) and heavily affected by RFI. The bias values for both I and Q channels are the nominal value 63.5. The number in the parentheses in the horizontal axis represents the actual radar center frequency, and the same applies to the subsequent figures.

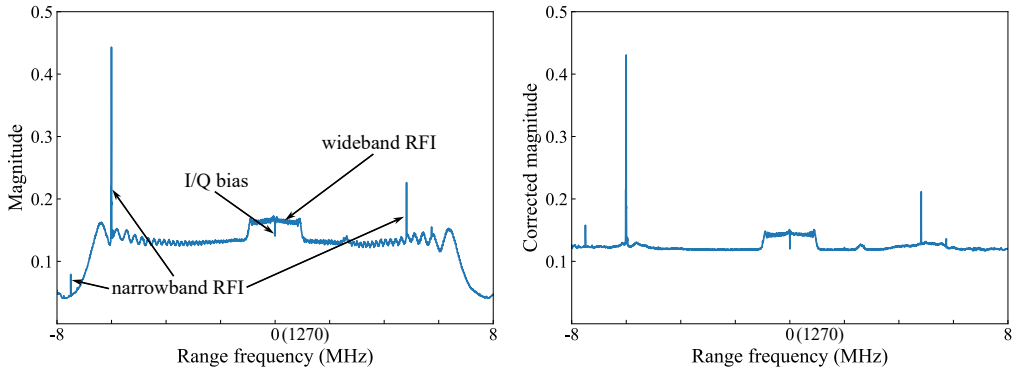

(a) (b)

Figure S2. Range spectra before (a) and after (b) removing spectrum magnitude fluctuations for a scene that is acquired by ALOS-1 in FBD mode (ALPSRP145510770-L1.0) and heavily affected by RFI. The bias values for the I and Q channels are estimated as the mean value of each channel.

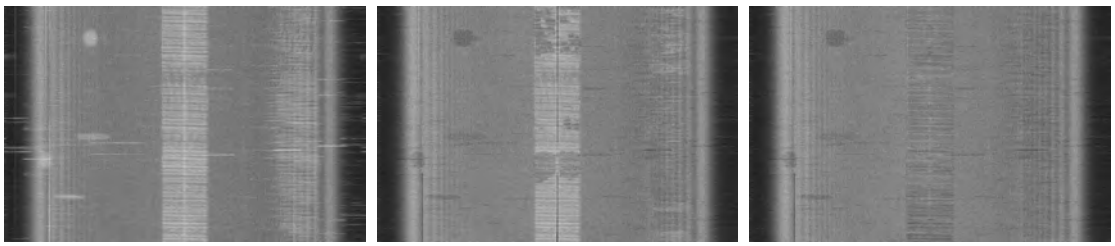

(a) (b) (c)

Figure S3. The improvement of cluster analysis on RFI detection results. (a) Range spectrum of the raw data before preprocessing. (b) Range spectrum after RFI detection and removal without clustering analysis. (c) Range spectrum after RFI detection and removal with clustering analysis.

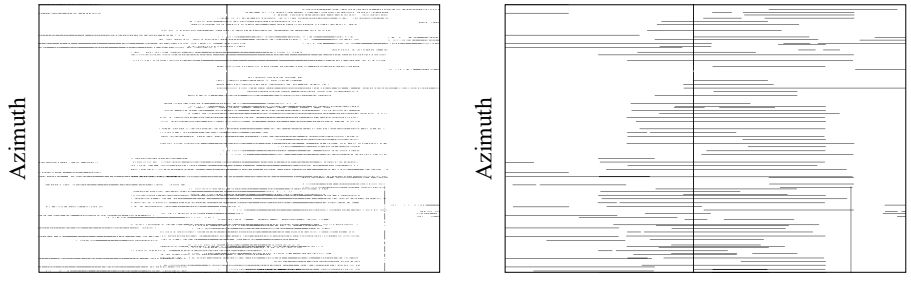

Figure S4. The improvement of morphological processing on RFI detection results. (a) Detection results without morphological processing. (b) Detection results with morphological processing.

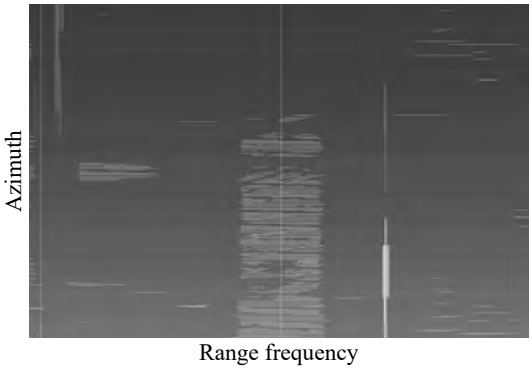

Figure S5. Part of the range spectrum reconstructed from a RFI record file.

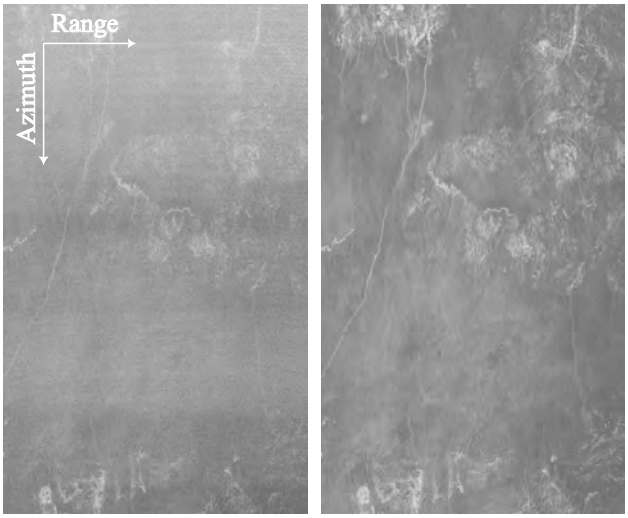

Figure S6. (a) SLC without RFI mitigation. (b) SLC with RFI mitigation.
(Generated from ALOS-1 raw data, ALPSRP263230860-H1.0)

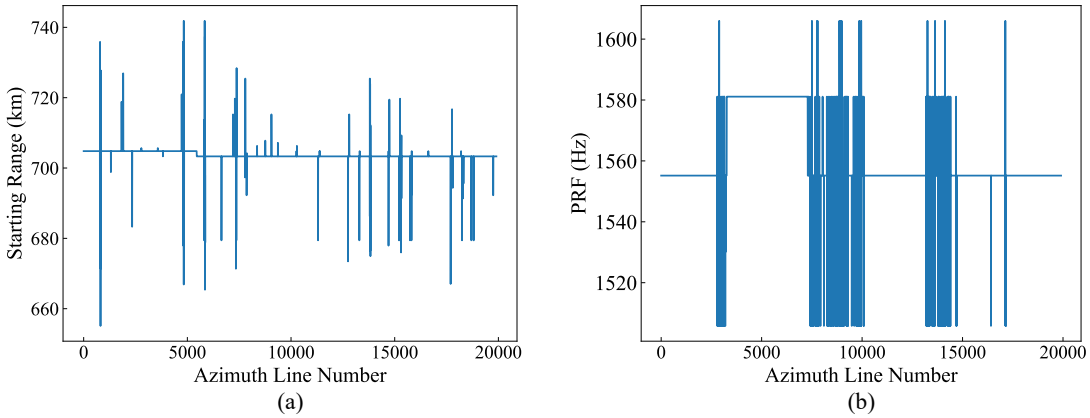

Figure S7. (a) Abnormal starting range values in JERS-1 raw data (J1SAR19970822M08202005476211_0000G006). (b) Abnormal PRF values in JERS-1 raw data (J1SAR19920427R01007705115219_0000G006.03).

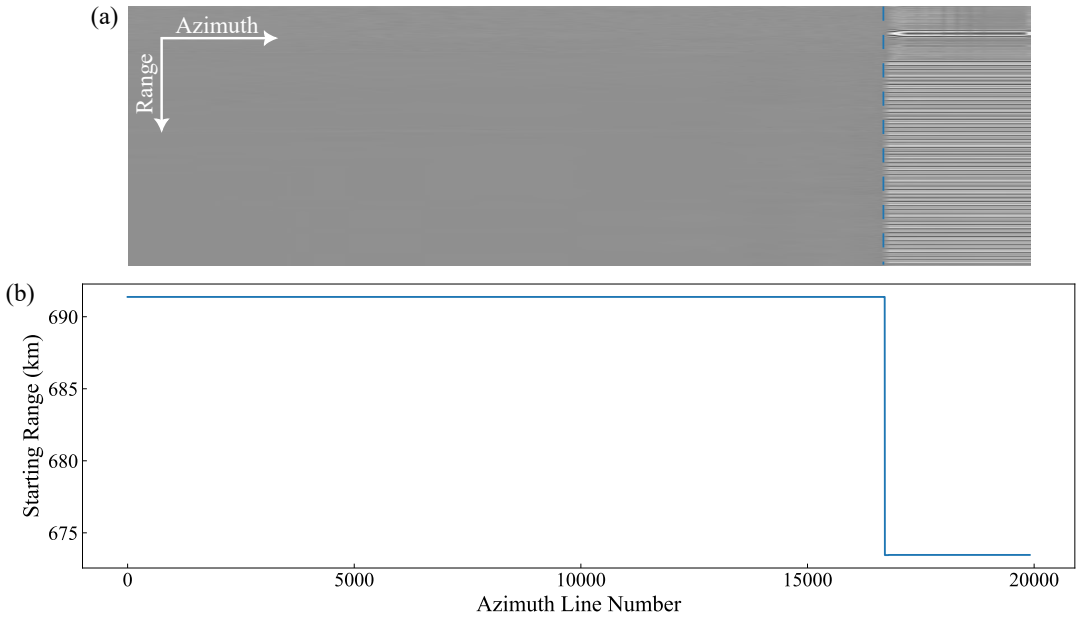

Figure S8. Abnormal radar echoes in JERS-1 raw data (J1SAR19950123R05107806145298_0000G006) (a) Magnitude of the raw data. (b) The corresponding starting range.

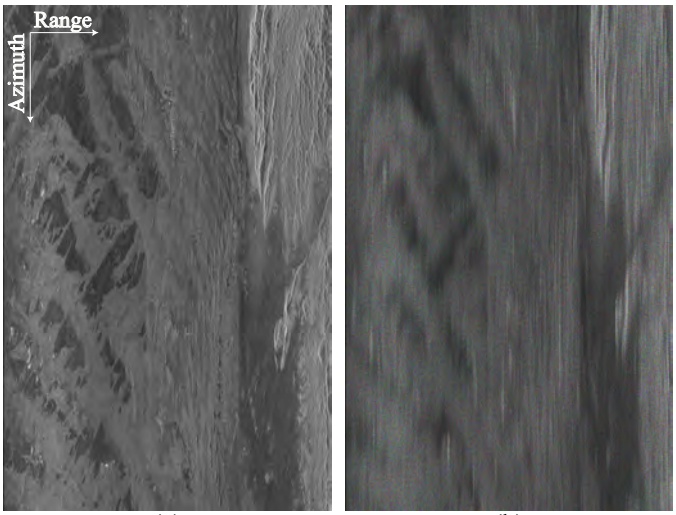

(a) (b)

Figure S9. (a) Original Envisat ASAR SLC. (b) SLC after azimuth defocusing. (ASA_IMS_1PNESA20070227_181332_000000152056_00013_26119_0000.N1)